HHS Public Access

Author manuscript

Cell Rep. Author manuscript; available in PMC 2022 June 24.

Published in final edited form as:

Cell Rep. 2022 May 31; 39(9): 110869. doi:10.1016/j.celrep.2022.110869.

Phosphatidylinositol transfer protein/planar cell polarity axis regulates neocortical morphogenesis by supporting interkinetic nuclear migration

Zhigang Xie[1,*],

Vytas A. Bankaitis[1,2,3,4,*]

[1]Department of Molecular & Cellular Medicine, Texas A&M Health Science Center, College Station, TX 77843, USA

[2]Department of Biochemistry & Biophysics, Texas A&M University, College Station, TX 77843, USA

[3]Department of Chemistry, Texas A&M University, College Station, TX 77843, USA

[4]Lead contact

SUMMARY

The neocortex expands explosively during embryonic development. The earliest populations of neural stem cells (NSCs) form a thin pseudostratified epithelium whose contour determines that of the adult neocortex. Neocortical complexity is accompanied by disproportional expansion of the NSC layer in its tangential dimension to increase tissue surface area. How such disproportional expansion is controlled remains unknown. We demonstrate that a phosphatidylinositol transfer protein (PITP)/non-canonical Wnt planar cell polarity (ncPCP) signaling axis promotes tangential expansion of developing neocortex. PITP signaling supports trafficking of specific ncPCP receptors from the NSC Golgi system to potentiate actomyosin activity important for cell-cycle-dependent interkinetic nuclear migration (IKNM). In turn, IKNM promotes lateral dispersion of newborn NSCs and tangential growth of the cerebral wall. These findings clarify functional roles for IKNM in NSC biology and identify tissue dysmorphogenesis resulting from impaired IKNM as a factor in autism risk, developmental brain disabilities, and neural tube birth defects.

Graphical abstract

*Correspondence: zxie@tamu.edu (Z.X.), vytas@tamu.edu (V.A.B.).

AUTHOR CONTRIBUTIONS

Z.X. and V.A.B. designed the experiments. Z.X. performed all experiments. Z.X. and V.A.B. interpreted the data and wrote the manuscript.

SUPPLEMENTAL INFORMATION

Supplemental information can be found online at https://doi.org/10.1016/j.celrep.2022.110869.

DECLARATION OF INTERESTS

The authors declare no competing interests.

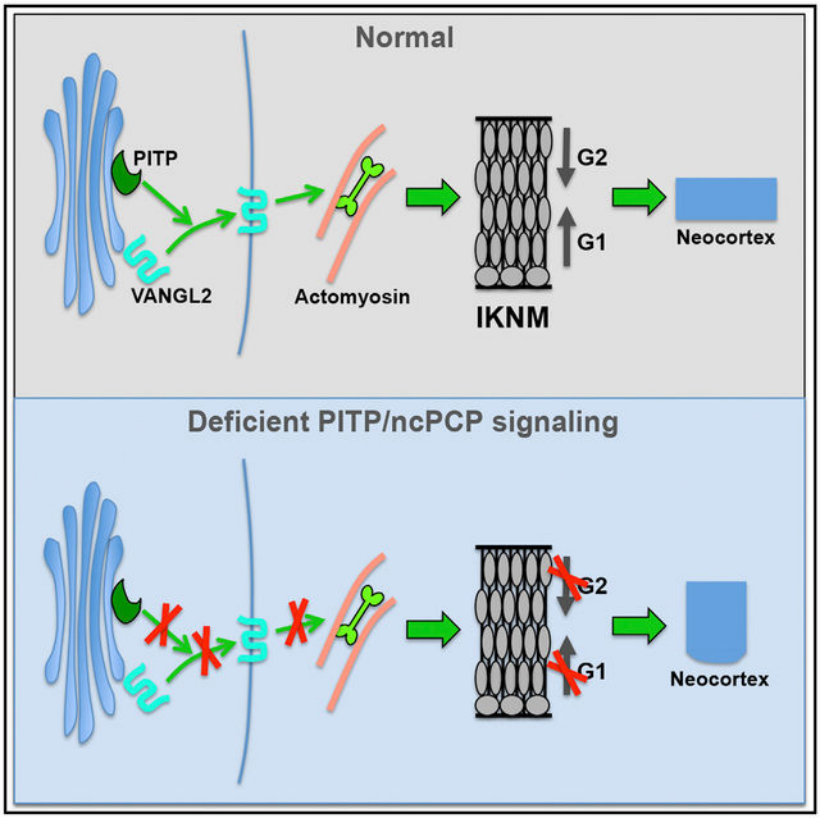

In brief

Xie and Bankaitis report that a phosphatidylinositol transfer protein/non-canonical planar cell polarity signaling axis supports interkinetic nuclear migration by promoting trafficking of specific non-canonical planar cell polarity receptors from the Golgi system to the plasma membrane, activating actomyosin, and supporting lateral expansion of the neocortex via a convergent extension mechanism.

INTRODUCTION

The neocortex is a mammalian-specific region of the brain that houses higher order functions such as cognition, perception, and language. Embryonic development of the neocortex is a complex process that integrates a number of highly regulated cell behaviors such as neural stem cell (NSC) self-expansion and self-renewal, neurogenesis, neuronal migration, and differentiation. The earliest NSC populations are neuroepithelial cells and their derivative apical radial glial cells (Taverna et al., 2014; Bonnefont and Vanderhaeghen, 2021). These NSCs span the entire neocortical wall and form a thin pseudostratified layer called the ventricular zone (VZ). It is from this tissue that the adult neocortex is built via the sequential generation and migration of progenitor cells, neurons, and glia (Taverna et al., 2014; Bonnefont and Vanderhaeghen, 2021). Thus, the surface contours of the adult neocortex are templated by the VZ contour. The importance of this developmental pathway is clear. Genetic defects affecting these processes are root causes of malformations of

cortical development (MCDs) that progress to intellectual disabilities (Hu et al., 2014; Juric-Sekhar and Hevner, 2019; Parenti et al., 2020).

Similar to cells in other pseudostratified tissues, NSCs exhibit characteristic cell-cycle-dependent nuclear movements called interkinetic nuclear migration (IKNM) (Reiner et al., 2012; Taverna et al., 2014; Miyata et al., 2015; Strzyz et al., 2016). Whereas NSC mitoses occur at the apical cell surface that contacts the ventricular fluid, NSC nuclei undergo a directed migration during G1 phase to a basal position where they reside during S phase. Subsequently, the nuclei reverse course and migrate back toward the apical NSC surface during G2. IKNM requires the activities of both the centrosome/microtubule/kinesin and the actin/myosin systems, and IKNM is known to play a role in the generation and tissue integration of neurons (Reiner et al., 2012; Taverna et al., 2014; Miyata et al., 2015; Strzyz et al., 2016). Yet how IKNM contributes to neocortical development, and how it is itself regulated, is not understood.

A striking morphological feature of the neocortex is its large surface area relative to its restricted thickness (Rakic, 2009; Lui et al., 2011; Florio and Huttner, 2014). The magnitude of this disproportional expansion correlates directly with mental capacity. The radial unit hypothesis links these basic principles of neocortical morphogenesis to higher order brain function (Rakic, 2009). This hypothesis describes the neocortex as a series of radial columns developed from founder NSCs within each column. Thus, neocortical surface area is determined by the number of radial columns. NSC self-expansion during early developmental stages is proposed to determine the number of radial units by organizing newborn NSCs into defined pools of radial column founder NSCs. Neocortical surface area reflects radial unit number which, in turn, determines mental capacity (Rakic, 2009; Lui et al., 2011; Florio and Huttner, 2014). However, it remains unexplained why NSC pool expansion across the *Mammalia* results in a progressively increase in founder NSCs at the expense of NSCs within each radial column.

Herein, we find that the disproportional expansion of the developing neocortex reflects an integration of phosphatidylinositol transfer protein (PITP) signaling, non-canonical planar cell polarity signaling (ncPCP) and IKNM in NSCs. Two highly homologous PITPs (PITPNA and PITPNB) support development of the mammalian neocortex (Xie et al., 2018). PITPNA and PITPNB do so by stimulating production of phosphatidylinositol-4-phosphate (PtdIns-4-P) pools on NSC *trans*-Golgi network (TGN)/endosomal membranes that recruit effector proteins to those compartments (Xie et al., 2018). We now show that PITPNA/PITPNB signaling is required for efficient trafficking of a subset of ncPCP receptors to the plasma membrane, and that the PITP/ncPCP axis promotes IKNM by regulating actomyosin activity. We further show impaired PITP/ncPCP-dependent IKNM disrupts neocortical surface expansion in the tangential dimension. The collective data report PITP/ncPCP-dependent IKNM potentiates a specialized form of convergent extension, a morphogenetic process that supports lateral distribution of newborn NSCs into formation of new radial columns at the expense of further populating existing radial columns. These data offer fresh perspectives into the etiologies of ASDs, intellectual disabilities, and birth defects associated with failures in neural tube closure.

RESULTS

PITP deficiencies result in dysmorphologies of the neocortex

The function of *Pitpna* and *Pitpnb* in dorsal forebrain was investigated at early stages of telencephalon development. These studies took advantage of a conditional gene eviction system induced by the *Emx1-Cre* driver that directs dorsal forebrain-specific deletion of floxed genes as early as embryonic day (E) 10.5 (Gorski et al., 2002; Liang et al., 2012; Insolera et al., 2014). Ablation of *Pitpna* and *Pitpnb* results in widespread apoptosis in the neocortex at E13.5 and later stages (Xie et al., 2018). At earlier stages apoptosis is mild, thus permitting interpretable analysis prior to E13. In that regard, the medial region of *Pitpna Pitpnb* double-knockout (DKO) neocortices was thicker and shorter in the mediolateral dimension compared with controls at early E12 (Figure S1A). This phenotype was further exaggerated by late E12 and was accompanied by a reversal in ventricular surface curvature from concave profiles in control neocortices to convex configurations in PITP DKO neocortices (Figure 1A). The reversal of surface contour was evident despite the fact that cells lining the ventricular surface were predominantly NSCs, as in the wild-type (WT) condition (Figure S1B). Moreover, NSC mitoses appropriately occurred along the ventricular surface in PITP DKO neocortex (Xie et al., 2018). The transformation of ventricular surface contour from a concave to a convex curvature suggested inappropriate accumulation of cell bodies/nuclei at the PITP DKO ventricular surface relative to the cell bodies/nuclei populating the deeper ventricular zone. As NSCs undergo IKNM, a process whereby newborn NSC nuclei migrate away from the ventricular surface, a potential factor for cell body/nucleus accumulation at the ventricular surface is impaired IKNM.

Cell cycle positioning of NSC nuclei is disorganized in PITP-deficient neocortex

To assess IKNM in PITP DKO neocortices, a pulse-chase experiment was performed to analyze NSC nuclear distribution during G1 and G2 phases of the NSC cell cycle *in vivo* (Figure 1B). Prior to harvesting, mouse embryos were sequentially labeled with 5-bromo-2'-deoxyuridine (BrdU), carboxyfluorescein succinimidyl ester (CFSE), and 5-ethynyl-2'-deoxyuridine (EdU). BrdU and EdU are thymidine analogs that label S-phase cells and are visualized by staining with MoBU-1 monoclonal antibody and click chemistry, respectively (Bradford and Clarke, 2011). CFSE is a fluorescent probe that labels mitotic NSCs in forebrain (Govindan et al., 2018). Cell cycle phase durations in medial mouse neocortex at E12.5 are estimated to be 3.3 h for G1, 4.9 h for S, and 2 h for G2+M (Miyama et al., 1997). Thus, BrdU, CFSE, and EdU labels were administered at 5, 2.5, and 1 h prior to embryo harvest, respectively. By this strategy, $CFSE^+$ cells identify newly divided NSCs in G1, EdU^+ cells represent S-phase NSCs (with a small fraction that just entered G2), and $BrdU^+EdU^-$ cells identify NSCs that exited S-phase 1–5 h prior to harvest. Performance of the G1 and G2 arms of NSC IKNM is inferred from the relative positions of $CFSE^+$ versus EdU^+ and EdU^+ versus $BrdU^+EdU^-$ somata, respectively.

Relative to $CFSE^+$ somata in WT neocortices, those in PITP DKO neocortices were positioned closer to the ventricular surface (Figures 1C and 1D); a PITP DKO NSC phenotype consistent with compromised nuclear migration away from the ventricular surface during G1. Two other observations were also consistent with impaired IKNM in PITP DKO

neocortex. First, the positions of PITP DKO EdU^+ nuclei were shifted toward the ventricular surface relative to WT controls (Figures 1E–1G). This rearrangement is also consistent with impaired migration during G1. A consequence of impaired migration during G1 is NSC entry into S phase before the nucleus reaches its normally basal position during that phase of the cell cycle. Second, the positions of $BrdU^+EdU^-$ nuclei in PITP DKO embryos exhibited significant basalward shifts relative to WT (Figures 1E, 1F, and 1H). This phenotype is consistent with retarded apical-directed nuclear migration in PITP DKO NSCs after entry into G2 phase.

Assessing IKNM defects in PITP-deficient neocortices by a quadruple-label strategy

To assess the distribution of NSC nuclei across the VZ by an independent method, we developed a quadruple-label immunostaining method for reliably distinguishing NSCs at different stages of the cell cycle in fixed brain sections. To that end, the positions of NSC nuclei (i.e. nuclei of $PAX6^+TBR2^-$ cells) were monitored at different phases of the cell cycle by co-immunostaining for PCNA and Ser10-phosphorylated histone H3 (pSer10). PCNA is expressed in all proliferating cells and exhibits signature cell-cycle-dependent nuclear distribution patterns. PCNA exhibits a diffuse nuclear localization in G1 and G2 cells but rearranges to a punctate localization profile during S phase (Ersoy et al., 2009; Leung et al., 2011; Schönenberger et al., 2015). Whereas pSer10 is commonly used as a marker for mitotic cells, it also marks G2-phase cells (Prigent and Dimitrov, 2003). Interestingly, pSer10 co-localized with the large majority of PCNA puncta, and its immunostaining intensity varied as a function of the cell cycle. Signal intensity was weak in NSCs with small nuclear PCNA puncta (i.e., in early and mid S-phase cells), was increased in NSCs with large nuclear PCNA puncta (late S-phase cells), was further intensified in NSCs with $pSer10^+$ nuclear puncta and diffuse nuclear PCNA, and was dramatically intensified in NSCs with pSer10-labeled chromatin (M-phase cells; Figure 2A). When coupled with demonstrations that both PCNA and pSer10 label centromeric regions (Prigent and Dimitrov, 2003; Nakagawa et al., 2016), and that PCNA distributions transformed from punctate to diffuse profiles upon entry into G2 (Ersoy et al., 2009; Leung et al., 2011; Schönenberger et al., 2015; Nakagawa et al., 2016), these profiles identified NSCs with large nuclear pSer10 puncta and diffuse nuclear PCNA as G2-phase cells (Figure 2B). NSCs marked by punctate nuclear PCNA were binned as S-phase cells regardless of pSer10 profile, and NSCs with diffuse nuclear PCNA staining and no detectable pSer10 fluorescence were classified as G1-phase cells (Figure 2B). By these criteria, late S- and G2-phase NSCs were unambiguously identified. Finally, G1- and early S-phase NSCs were confidently recognized in the apical quartile of the VZ, as this is a region where mid to late S-phase cells are rare.

Late S-phase NSC nuclei ($PAX6^+TBR2^-$) were distributed primarily in the basal half of the VZ in WT neocortex (Figures 2C–2E), G2-phase NSC nuclei were predominantly distributed throughout the apical half of the VZ (Figures 2C, 2D, and 2F), and M-phase NSC nuclei lined the ventricular (apical) surface (Figure 2D). Those observations are consistent with previous IKNM models in which M-phase nuclei localize to the ventricular surface, migrate in a basally directed fashion to the upper VZ during G1, complete S phase in the basal VZ, and subsequently retreat back toward the ventricular surface during G2. As such, these results validate the approach.

Consistent with the results of the pulse-chase experiments, the PCNA profile revealed increased numbers of early S-phase nuclei in the apical half of PITP DKO neocortices compared with WT (Figure S2). An additional three observations diagnosed impaired IKNM in PITP DKO neocortices. First, whereas late S-phase DKO NSC nuclei remained distributed predominantly in the basal VZ (Figures 2C–2E), G2-phase NSC nuclei failed to populate the apical VZ (Figures 2C, 2D, and 2F). Second, relocalization of NSC nuclei toward the ventricular surface during the late S-to-G2 transition was compromised (Figure 2G). Third, the fractional representation of G1/early S-phase NSC nuclei was elevated in the ventricular quartile of the VZ (Figure 2H). Thus, PITP deficiencies (1) impair apically directed migration of G2-phase NSC nuclei toward the ventricular surface and (2) impair basally directed migration of G1-phase NSC nuclei toward the VZ/subventricular zone boundary.

PITP-deficient NSCs remain in contact with the ventricular surface

As PITPNA/PITPNB play an essential role in radial alignment of NSCs (Xie et al., 2018; Grabon et al., 2019), we considered the possibility that the apparent IKNM defects reflect some indirect manifestation of NSC crowding and subsequent delamination. Detached NSCs might subsequently migrate away from the ventricular surface to upper neocortical layers (Okamoto et al., 2013). Thus, the morphologies of NSCs were examined by z series confocal images of EGFP-transfected NSCs. Serial imaging profiles clearly showed that the apical process of NSCs remained attached to the ventricular surface in DKO neocortex (Figure S3A). For NSCs whose entire apical process was viewed in the z series, frequencies of NSC delamination from the apical surface were equally rare in both WT and PITP DKO neocortices (WT, 0.76% ± 0.45%; PITP DKO, 0.74% ± 0.44%; n = 4 embryos for each group; $p = 0.97$, Student's t test).

In independent experiments, immunostaining of the apical tip junction protein ZO-1 also reported no enhancement in apical tip detachment from the ventricular surface in the PITP DKO medial neocortex relative to WT (Figure S3B). Unexpectedly, ZO-1 imaging revealed that the PITP DKO ventricular surface in this region was abnormally serrated (Figure S3B). The thickened medial neocortices of PITP DKO embryos indicate abnormal NSC densities in the mediolateral dimension. As the apical tips of those NSCs remained attached to the ventricular surface, enhancements in NSC density must translate into elevated apical tip densities at the ventricular surface. Thus, a serrated ventricular surface suggests a delamination-independent mechanism by which PITP DKO neocortex compensates for apical tip crowding.

PITP deficiencies lead to impaired lateral distribution of newborn NSCs

In addition to IKNM defects, the altered shape of PITP DKO medial neocortex suggested that preferential distribution of newborn NSCs in the lateral dimension was retarded. To test this possibility, we identified newborn NSCs generated from a single mother NSC in the medial neocortex and assessed the dispersion of the newborn NSCs in the mediolateral dimension. An EGFP plasmid was first electroporated into the medial neocortex of control or PITP DKO embryos at E11.5, an mCherry plasmid was then electroporated into the same region 7 h later, and electroporated embryos were harvested for analysis 17 h later

(Figure 3A; Xie et al., 2016). Because doubly transfected NSCs are very rare, these NSCs are initially distributed as well-dispersed single cells within the neocortex. After 1–3 cell divisions, the progeny from those isolated doubly transfected NSCs form distinct clusters of $EGFP^{+}mCherry^{+}$ cells. The span of the cluster in the mediolateral versus the radial axis reports the primary distribution vector.

The specific time frame of this experiment was chosen to ensure that the impact of PITP deficiencies on NSC distribution would be observed in the E11.5–E12.5 window. Because of the short cell cycle length at E11.5–E12.5 (8.1–10.2 h) (Miyama et al., 1997), initially transfected NSCs were estimated to have completed 1–3 rounds of division at the time of analysis. Differentiated progeny of those transfected NSCs, such as $TBR2^{+}$ intermediate progenitor cells (IPCs) and neurons ($PAX6^{-}TBR2^{-}$), were excluded from the analysis. The data show that the span of the $EGFP^{+}mCherry^{+}$ NSC clusters in the mediolateral dimension was strongly reduced in PITP DKO neocortex compared with WT (Figures 3B and 3C). This reduction was not due to variations in cluster sizes, which were similar between WT (2.81 ± 0.19, mean ± SD; $n = 31$) and PITP DKO neocortices (2.51 ± 0.13; $n = 45$; $p = 0.65$ compared with control, Student's t test). We conclude that lateral dispersion of newborn NSCs is impaired in PITP-deficient neocortex.

The association of impaired IKNM and reduced dispersion of NSCs in the lateral dimension recapitulated hallmark features of convergent extension, that is, a tissue morphogenetic process used in multiple developmental contexts to elongate developing tissues in one dimension and narrow the tissue in another (Shindo, 2018; Sutherland et al., 2020). As IKNM generates two opposing forces, a basally directed force defined by migrating G1 nuclei and an opposing apically directed force defined by migrating G2 nuclei, IKNM is an attractive candidate for driving convergent extension in the developing neocortex. During early neocortical development, the neocortex is composed largely of proliferating NSCs that actively undergo IKNM. Thus, inefficient IKNM would effect large-scale reductions in cell intercalation in the radial dimension. These deficits would result in increased tissue thickness and decreased extension in the tangential dimension observed in PITP DKO neocortex.

The *loop tail (lp) Vangl2* allele phenocopies impaired IKNM of PITP-deficient NSCs

The ncPCP pathway is an evolutionarily conserved signaling circuit required for convergent extension (Shindo, 2018; Sutherland et al., 2020). Thus, a convergent extension model for IKNM predicts that the ncPCP pathway is required for IKNM and neocortical morphogenesis. This prediction was interrogated using several approaches that examined whether specific ablation of the ncPCP pathway recapitulated the neocortical and IKNM derangements observed for PITP DKO embryos. These approaches focused on receptors that specifically promote ncPCP signaling and do not participate in the canonical Wnt/β-catenin pathway (i.e. VANGL1/2, CELSR1/2/3, PTK7) (Butler and Wallingford, 2017; Humphries and Mlodzik, 2018).

Examination of homozygous $Vangl2^{lp/lp}$ embryos at E12.5 revealed severe anatomical defects in the CNS. These included failures in neural tube closure (Murdoch et al., 2001, 2014) and rupture of the neocortex (Figure S4A). We also noted that increased neocortex

thickness and a convex ventricular surface were common features in intact areas of the *Vangl2*$^{lp/lp}$ neocortex. These features were particularly striking in the medial neocortex (Figure 4A). Alterations in neocortical length in the mediolateral dimension were not assessed, because the derangement of overall forebrain morphology in mutant embryos precluded such analyses. However, IKNM defects were obvious in those thickened regions of the neocortex, as indicated by (1) altered spatial distributions of G2 NSC nuclei but not of late S-phase NSC nuclei (Figures 4B–4D), (2) marked reductions in apical-directed migration of G2-phase nuclei toward the ventricular surface (Figure 4E), and (3) pronounced accumulation of G1/early S-phase NSC nuclei in the apical quartile of the VZ (Figure 4F).

Altered apical surface curvature and impaired IKNM in *Vangl2*$^{lp/lp}$ neuroepithelial tissues

The neocortical shape changes in *Vangl2*$^{lp/lp}$ embryos were not indirect effects associated with failures to close the neural tube, or with rupture of the neocortex. Other developing *Vangl2*$^{lp/lp}$ neuroepithelial tissues similarly reconfigured their ventricular surfaces from concave to convex curvatures. First, the epithalamus and dorsal thalamus neuroepithelia in *Vangl2*$^{lp/lp}$ mutant embryos exhibited pronounced folding of the inner surface (Figure S4B) and impaired IKNM (Figure S4C). This dysmorphology cannot be explained by passive space filling of an open ventricle as the space in this area is restricted, even in WT embryos (Figure S4B). Second, the convex curvature of the apical surface was apparent in neural tubes of mutant embryos as early as E8.5–E9.0 (Figure S4D); i.e., stages that precede caudal neuropore closure (which occurs at E9.5–E10.0; Chen et al., 2017). Imposition of convex curvature was accompanied by increased numbers of early G1-phase nuclei at the apical surface (Figure S4D). We were unable to monitor neural tube IKNM at these early stages because of tissue thinness. Nevertheless, consistent transitions from concave to convex curvatures were observed for apical surfaces of the (1) neocortex, (2) epithalamus/dorsal thalamus, and (3) neural tube, all of which report impaired relocation of newborn NSC somata away from the apical site of mitosis in *Vangl2*$^{lp/lp}$ embryos.

The *ctb Celsr1* allele phenocopies impaired IKNM of PITP-deficient NSCs

Embryos homozygous for the curly tail bobber (*ctb*) allele of the ncPCP receptor *Celsr1* were analyzed for IKNM defects and neocortical morphology. This mutant mouse carries a null allele where a translational frameshift induces downstream nonsense-mediated mRNA decay (Harris et al., 2016). Consistent with previous reports of incomplete penetrance of tissue defects in *Celsr1*-null mice (Ravni et al., 2009; Qu et al., 2010), 53% of *Celsr1*$^{ctb/ctb}$ embryos (18 of 34) presented open neural tube defects. Because the lack of neural tube defects in some nullizygous embryos likely reflects active compensatory mechanisms (Murdoch et al., 2014), analyses were restricted to mutant embryos with neural tube defects.

Celsr1$^{ctb/ctb}$ homozygotes exhibited neocortical dysmorphologies and IKNM deficits that were indistinguishable from those recorded for *Vangl2*$^{lp/lp}$ embryos. The cardinal phenotypes included (1) rupture of the neocortex (Figure S5A); (2) thickening of medial neocortex with a convex ventricular surface (Figure S5B); (3) reduced distribution of G2, but not late S-phase, NSC nuclei in the apical VZ (Figures S5C–S5E); (4) decreased shift of nuclear position toward the ventricular surface during NSC transition from late S to G2 phase of the cell cycle (Figure S5F); and (5) accumulation of G1- and early S-phase NSC

nuclei in the apical quartile of the VZ (Figure S5G). Thus, both *Vangl2*$^{lp/lp}$ and *Celsr1*$^{ctb/ctb}$ mutant embryos shared similar defects in neocortical morphogenesis and IKNM consistent with a convergent extension model for IKNM. Moreover, both phenocopied the defects recognized in PITP DKO neocortex.

Neocortical dysmorphology and impaired IKNM in a mosaic model for ncPCP deficiency

The *Vangl2*$^{lp/lp}$ and *Celsr1*$^{ctb/ctb}$ data were buttressed by studies assessing whether functional interference with a third receptor specific to the ncPCP pathway (PTK7) phenocopied the defects in neocortical morphogenesis and IKNM scored for PITP DKO, *Vangl2*$^{lp/lp}$, and *Celsr1*$^{ctb/ctb}$ mutant embryos. In these studies, we adopted an experimental regime that did not rely on analyses of mutant mice. Rather, a regional mosaicism was induced by introducing a dominant-negative *Ptk7* allele into WT E12.5 neocortex by *in utero* electroporation. This *Ptk7* allele encodes a truncated form of the receptor that lacks the cytoplasmic tail (PTK7ΔC) (Lu et al., 2004; Gärtner et al., 2014). Neocortical morphology and IKNM were assessed after 24 h. As a high fractional representation of electroporated NSCs is required to influence neocortex morphology, only embryos with high transfection efficiencies were analyzed. PTK7ΔC expression induced local deformation of the concave ventricular surface to a convex contour and evoked tissue thickening in efficiently transfected regions (Figure 5A). Moreover, PCNA/pSer10 co-immunostaining demonstrated that those thickened regions of the neocortex exhibited impaired IKNM (Figures 5B–5F). Thus, interfering with ncPCP signaling in a restricted region of an otherwise WT neocortex was sufficient to evoke local dysmorphologies and IKNM defects that phenocopied those recorded for PITP DKO, *Vangl2*$^{lp/lp}$, and *Celsr1*$^{ctb/ctb}$ embryos.

PITP DKO neocortices exhibit cargo-specific ncPCP receptor trafficking defects

PITPs potentiate Ptdns-4-P-dependent membrane trafficking from the TGN system (Grabon et al., 2019), suggesting that non-canonical Wnt/PCP signaling is impaired in PITP-deficient NSCs because of compromised membrane trafficking of one or more ncPCP receptors from the TGN. Indeed, although a significant fraction of VANGL2 localized to the plasma membrane, a pronounced accumulation of an intracellular pool of VANGL2 was recorded in PITP DKO NSCs. The compartment of accumulation co-localized with the TGN marker GOLGIN97 (Figure 6A). VANGL2 antibody specificity was verified by the loss of immunoreactivity in neocortex expressing the unstable *lp* mutant form of VANGL2 (Figure S6A). This TGN membrane trafficking defect was also evident in PITP DKO embryos for VANGL1 (Figure S6B). By contrast, no such intracellular pools of PTK7 were detected in PITP DKO neocortex (Figure S6C), and the subcellular distribution of FZD2 (a receptor shared by the canonical Wnt and non-canonical Wnt/PCP signaling pathways) was also unperturbed in PITP DKO NSCs (Figure S6D). These data report that membrane trafficking efficiency of a subset of ncPCP receptors from the late Golgi system to the plasma membrane was impaired in PITP DKO neocortices.

ncPCP receptor membrane trafficking defects are cell-autonomous phenotypes

To determine whether VANGL2 membrane trafficking defects in PITP DKO neocortex represented cell-autonomous NSC phenotypes, the *Pitpna* and *Pitpnb* genes were ablated in a subset of NSCs residing in an otherwise WT neocortical niche. In these experiments,

EGFP and Cre plasmids were co-introduced into E12.5 neocortices of *Pitpna*$^{fl/fl}$ *Pitpnb*$^{fl/fl}$ embryos by *in utero* electroporation. Cre expression in individual transfected NSCs (marked with EGFP) induced deletion of both floxed *Pitpna* and *Pitpnb* alleles in those cells, whereas neighboring non-transfected NSCs remained competent for both *Pitpna* and *Pitpnb* gene expression (Xie et al., 2018). As recorded for PITP DKO neocortex, intracellular pools of VANGL2 accumulated in GOLGIN 97-marked TGN compartments of transfected NSCs (Figures 6B–6D). Such accumulations were not evident in adjacent untransfected NSCs where VANGL2 decorated the plasma membrane exclusively (Figure 6C). Thus, the inefficiencies in VANGL2 trafficking from the TGN of PITP DKO NSCs reported a cell-autonomous phenotype.

Effector specificity in trafficking of ncPCP receptors from NSC TGN/endosomes

PITP-dependent PtdIns-4-P synthesis on the TGN promotes anterograde cargo trafficking by stimulating signaling pathways that enable efficient recruitment of PtdIns-4-P binding proteins/effectors to TGN membranes. One candidate for such an effector is GOLPH3, a peripheral membrane protein of TGN/endosomes whose role in promoting vesicle budding from the TGN is mediated via its interaction with the non-conventional actin-based motor Myo18A (Kuna and Field, 2019). Moreover, GOLPH3 recruitment to NSC TGN membranes requires PITP-dependent PtdIns-4-P signaling, and this localization is essential for maintenance of NSC polarity in developing neocortex (Xie et al., 2018). Surprisingly, using an *in utero* electroporation regime, we found that functional silencing of GOLPH3 in transfected NSCs did not impair VANGL2 trafficking from TGN/endosomal membranes (Figure S6E). These data indicate that although PITPs potentiate cell-autonomous VANGL2 trafficking from the TGN, they do so by a mechanism that exhibits cargo specificity and is largely independent of GOLPH3 activity.

The PITP/ncPCP axis maintains actomyosin activity in the nuclear periphery

How does PITP/ncPCP support IKNM? ncPCP signaling promotes tissue convergent extension by regulating the actomyosin cytoskeleton (Devenport, 2014; Shindo, 2018), and actomyosin activity is a major driving force for IKNM (Norden et al., 2009; Leung et al., 2011; Schenk et al., 2009). To determine whether and how actomyosin activity contributes to PITP/ncPCP-dependent IKNM, we compared Ser19-phosphorylated (pSer19) myosin regulatory light chain 2 (MRLC2) immunoreactivity in WT versus PITP DKO neocortex. pSer19 MRLC2 is a reporter for an activated actomyosin system. In WT neocortex, intense punctate pSer19 immunoreactivity was evident along the ventricular surface. Less intense punctate pSer19 immunoreactivity was also detected surrounding WT NSC nuclei within the VZ (Figure 6E). Although PITP DKO neocortices largely preserved the intense pSer19 MRLC2 immunoreactivity along the ventricular surface, the signal surrounding the nuclear periphery was essentially absent (Figure 6E). Those profiles were reproduced in *Vangl2*$^{lp/lp}$ VZ (Figure 6F). These data are consistent with actomyosin activity in the nuclear periphery representing a downstream effector of the PITP/ncPCP axis in promoting IKNM and proper neocortical morphogenesis.

Interfering with actomyosin activity phenocopies neocortical and IKNM defects

The possibility that actomyosin activity is a key downstream effector that links PITP/ncPCP signaling with IKNM and neocortical morphogenesis was further interrogated using an *in utero* electroporation approach. A nonphosphorylatable version of the myosin light chain regulator MRLC2 was expressed in individual NSCs of E11.5 neocortex. This double mutant (MRLC2-AA) is an inhibitor of actomyosin activation (Komatsu et al., 2000; Fumoto et al., 2003; Vicente-Manzanares et al., 2009). The embryos were harvested 20 h after electroporation and analyzed for actomyosin activity, neocortical morphology, and IKNM.

Indeed, MRLC2-AA expression suppressed actomyosin activity around the nuclear periphery and at the apical tip of transfected NSCs (Figure S7). Moreover, the neocortical dysmorphologies and IKNM defects observed in PITP DKO embryos were recapitulated in highly mosaic neocortical regions where electroporation with the MRLC2-AA expression plasmid was highly efficient (Figures 7A–7F). To determine whether MRLC2-AA inhibited lateral distribution of newborn NSCs, a two-step electroporation experiment was performed similar to that used for analysis of NSC lateral dispersion in PITP DKO embryos (see above). This experiment was performed with the modification that the MRLC2-AA plasmid was co-electroporated with the EGFP plasmid in the first step. Compared with mock controls using EGFP plasmid alone, the lateral dispersion of doubly transfected NSCs in the MRLC2-AA group was inhibited (Figures 7G and 7H). This defect did not reflect variations in cluster sizes. These remained similar between control and MRLC2-AA groups (2.81 ± 0.19 [mean ± SD], n = 31 vs 2.67 ± 0.25 [mean ± SD], n = 24, respectively; p = 0.65, Student’s t test).

DISCUSSION

Herein, we describe a critical role for a PITP/ncPCP signaling axis in regulating neocortical morphogenesis. The basic outline of this signaling circuit is as follows. PITP-dependent PtdIns-4-P signaling in the NSC TGN/endosomal system supports efficient membrane trafficking of a subset of ncPCP receptors to the plasma membrane. Efficient execution of the trafficking program ensures sufficient ncPCP signaling to promote IKNM by stimulating actomyosin activity at the nuclear periphery and perhaps the ventricular surface (Figure 7I). Thus, IKNM supplies a mechanical force that ensures newborn NSCs are preferentially distributed in the lateral dimension of the VZ as new radial unit founder NSCs, rather than in the radial dimension, to increase NSC numbers within each radial unit. This pathway interprets PITP/ncPCP-dependent IKNM as an essential feature of a form of convergent extension that endows the VZ with the intrinsic ability to remain thin. This structural feature of the VZ then templates the morphology of adult neocortex as a thin tissue sheet.

PITP/ncPCP signaling promotes IKNM to drive a form of convergent extension

IKNM occurs in pseudostratified epithelial tissues, and several hypotheses suggest why IKNM is important for development of those tissues. These proposals include IKNM providing (1) space for cell rounding during mitosis, (2) a mechanism for improved nuclear access to signaling molecules/growth factors in the lateral ventricular fluid that bathes the apical NSC tip, (3) a means for fostering centrosome-nucleus contact during mitosis, and (4)

an appropriate integration of differentiated daughter cells into the tissue (Reiner et al., 2012; Taverna et al., 2014; Miyata et al., 2015; Strzyz et al., 2016). However, the role IKNM plays in tissue morphogenesis remains unresolved.

The increased thickness and decreased length of the PITP DKO neocortex, when coupled with the results of two independent assays that quantify distribution of NSC nuclei as a function of cell cycle phase, report an impaired IKNM. This interpretation is strengthened by our demonstration that the apical tips of PITP DKO NSCs do not detach from the ventricular surface, thereby excluding an indirect effect of PITP dysfunction on the disorganization of the cell cycle-specific distribution of NSC nuclei in the VZ. These collective observations provide an interesting direction from which to interpret the biological function of IKNM in neocortical development, namely, that IKNM is a major mechanism for determining neocortical morphogenesis by channeling the distribution of newborn NSCs via a specialized form of convergent extension.

Three lines of evidence support this view. First, *in utero* electroporation experiments demonstrated restricted distribution of newborn NSCs along the mediolateral axis in PITP DKO neocortex. Second, loss of function in two receptors that specifically promote ncPCP signaling (*Vangl2*$^{lp/lp}$ and *Celsr1*$^{ctb/ctb}$) recapitulated the IKNM and neocortical thickening phenotypes of PITP DKO mutants. Third, regionally mosaic expression of a dominant-negative version of a third ncPCP receptor (PTK7ΔC), in an otherwise WT neocortex, induced similar morphological and IKNM derangements. It remains unclear why IKNM defects and neocortical shape changes were most pronounced in the medial neocortex of PITP DKO, *Vangl2*$^{lp/lp}$ and *Celsr1*$^{ctb/ctb}$ mutant embryos. Whether these phenotypes reflect the action of regionally specific mechanisms for promoting IKNM, or whether functional compensation pathways differ in the lateral vs medial neocortex of PITP DKO, *Vangl2*$^{lp/lp}$, and *Celsr1*$^{ctb/ctb}$ embryos, is an open question.

PITPs and membrane trafficking of ncPCP receptors

How does PITP function interface with ncPCP signaling? PITPs regulate membrane trafficking through the TGN by coordinating PtdIns-4-P signaling with PtdCho metabolism (Cleves et al., 1991; Schaaf et al., 2008; Xie et al., 2018; our unpublished data). We therefore interpret the cell-autonomous VANGL1/2 trafficking defects recorded for PITP DKO NSCs as reflective of PtdIns-4-P signaling defects in the TGN system of PITP-deficient NSCs. In that regard, the two unexpected findings encountered in this study were the cargo and effector specificity of these defects. First, trafficking of only a subset of ncPCP receptors was compromised in PITP DKO NSCs. This phenotype, although consistent with the viability of the PITP-deficient NSCs, nonetheless argues against models that presume all exocytic cargoes are exported from the TGN in an equally PtdIns-4-P-dependent manner (Waugh, 2019). An alternative interpretation is distinct TGN cargos exhibit different threshold requirements for PtdIns-4-P signaling in order to be efficiently exported from the TGN.

The apparent PtdIns-4-P effector specificity in ncPCP receptor trafficking was also unexpected. GOLPH3 is a PtdIns-4-P effector proposed to be a core component of the TGN trafficking machinery (Kuna and Field, 2019). However, GOLPH3-deficient NSCs are viable

and efficiently traffic VANGL2. We interpret these data to indicate other PtdIns-4-P effectors are the primary drivers of VANGL2 trafficking from the TGN to the plasma membrane. The cargo and effector specificity we document here argue for the existence of functionally dedicated PtdIns-4-P pools in the TGN rather than some bulk pool commonly accessed by all PtdIns-4-P effectors. The ideas of PtdIns-4-P pool diversity and effector specificity suggest mechanisms whereby distinct PtdIns-4-P effectors engage with dedicated PtdIns-4-P pools to engineer what is in effect point resolution to PtdIns-4-P signaling on the TGN surface (Grabon et al., 2019).

Although PITP DKO embryos and ncPCP-deficient embryos exhibit similar defects in IKNM and neocortical tissue thickness/convexity, neocortical phenotypes are not identical between those embryos. This can be accounted for by several factors. First, ncPCP-deficient embryos exhibit open neural tube defects that indirectly affect neocortical shape by eliminating the cerebrospinal fluid pressure. Neural tube defects are not expected to occur in PITP DKO embryos as both genes are specifically evicted from dorsal forebrain only. Second, impaired trafficking of ncPCP receptors in PITP DKO embryos reduces, but does not eliminate, ncPCP receptor function. By the same token, PITP DKO neocortices present their own signature phenotypes (loss of radial polarity, TGN redistribution, apoptosis) not exhibited by ncPCP receptor-deficient NSCs. PITPs regulate other aspects of TGN PtdIns-4-P signaling in addition to trafficking of specific ncPCP receptors. In terms of IKNM involvement, however, our findings with other neuroepithelial tissues in *Vangl2*$^{lp/lp}$ embryos, and on the impact of expressing a dominant-negative PTK7 on the shape of otherwise WT neocortex, indicate that impaired IKNM is a significant contributor to altered neocortical shape in ncPCP-deficient embryos.

Actomyosin activation links the PITP/ncPCP axis to IKNM

A common phenotype of both PITP DKO NSCs and NSCs deficient in ncPCP receptor activity (i.e., *Vangl2*$^{lp/lp}$ mutants) is loss of actomyosin activity at the nuclear periphery. Given that actin dynamics contribute to the forces that drive IKNM (Taverna et al., 2014; Strzyz et al., 2016), we interpret these data to indicate that the PITP/ncPCP pathway couples cell adhesion signaling inputs at the NSC somata with modulation of actin cytoskeleton dynamics in the environment of the NSC nucleus. Compromised trafficking to the plasma membrane of ncPCP pathway receptors diminishes these cytoskeleton-based forces and thereby impairs IKNM.

Our observation that MRLC2-AA expression suppressed actomyosin activity in the nuclear periphery and at the apical tip of transfected NSCs, when coupled with the known role of ncPCP in cell-cell junction remodeling (Shindo, 2018), is also consistent with actomyosin activity at the ventricular surface contributing to IKNM. PITP/ncPCP-regulated remodeling of the mesh-like F-actin structure at the apical tip plasma membrane might also facilitate lateral dispersion of newborn NSCs (Figure 7I). Our data cannot formally exclude this possibility, as the immunostaining strategy used to address the question might not exhibit sufficient sensitivity for detecting subtle alterations in actomyosin activity at the ventricular surface.

IKNM-dependent NSC organization, developmental disabilities, and birth defects

Our demonstration that PTK7 regulates IKNM, and consequently NSC organization and neocortical surface curvature, is of interest as PTK7 is a high-confidence autism risk gene (Basa et al., 2009). These findings suggest that impaired IKNM is an unappreciated contributor to developmental brain disabilities. In support of this idea, a number of autism risk or intellectual disability-associated genes encode proteins that are attractive candidates for regulating IKNM during NSC self-expansion (Basa et al., 2009). These include *DYNC1H1* (dynein cytoplasmic 1 heavy chain 1), *KIF14* (kinesin family member 14), *MYH10* (myosin heavy chain 10), *PRICKLE1* and *PRICKLE2* (prickle planar cell polarity proteins 1 and 2), and *PAFAH1B1* (platelet activating factor acetylhydrolase 1b regulatory subunit 1). Indeed, *PAFAH1B1* patients are among the most studied cases of inherited intellectual disabilities. These patients consistently present reduced gyrification and increased thickness of the lissencephalic neocortex (Di Donato et al., 2017). Although *PAFAH1B1*-associated intellectual disabilities are traditionally interpreted in the context of deranged neuronal migration, the *PAFAH1B1* gene product regulates nuclear migration in NSCs (Tsai et al., 2005). Thus, convergent extension models featuring IKNM as a critical determinant of neocortical thickness provide an original perspective for why neocortical thickness is increased in *PAFAH1B1*-deficient patients.

Finally, although this study focuses on the neocortex, our conclusions also offer fresh insights into the etiologies of neural tube defects. These developmental pathologies rank among the most common human birth defects. A major cause of open neural tube defects in humans is impaired ncPCP pathway activity. The prevailing interpretation of those data is that the neural plate fails to undergo convergent extension in the face of insufficient ncPCP signaling. This defect results in production of an abnormally wide neuroepithelial tissue that subsequently impedes neural tube closure (Butler and Wallingford, 2017; Shindo, 2018). We offer an alternative perspective. Our data indicate that the apical surfaces of ncPCP-deficient neuroepithelial tissues have intrinsic tendencies to assume convex curvatures because of impaired relocation of newborn nuclei away from the site of mitosis. We suggest that adoption of convex curvature by the apical surface of the neuroepithelium imposes a geometric constraint of sufficient magnitude to prevent neural tube closure.

Limitations of the study

Herein we present a model in which PITP/ncPCP signaling promotes lateral expansion of the cerebral wall during early stages of development by supporting IKNM. Several mechanistic issues remain unresolved by this model. These include (1) the molecular basis for selective trafficking defects of a subset of ncPCP receptors under conditions of PITP/PtdIns-4-P-deficit, (2) the mechanisms by which actomyosin dynamics at the NSC nuclear periphery (and the ventricular surface?) contribute to PITP/ncPCP-dependent IKNM, and (3) the basis for why morphogenesis of the medial neocortex is more sensitive to deficits in PITP/ncPCP-dependent IKNM than is the lateral neocortex. Finally, the linkage between PITP and ncPCP signaling is unlikely to be strictly linear. On one hand, PITP-dependent PtdIns-4-P-deficiencies affect other pathways (e.g., GOLPH3 signaling and the trafficking of other cell surface receptors). On the other, ncPCP signaling regulates NSC functions independent of PITP/PtdIns-4-P signaling. This complex relationship, along with variable

signaling outputs associated with deficits in each system, likely account for why neocortical phenotypes exhibited by PITP DKO and ncPCP-deficient embryos differ in key respects.

STAR★METHODS

RESOURCE AVAILABILITY

Lead contact—Further information and requests for resources and reagents should be directed to and will be fulfilled by the Lead Contact, Vytas A. Bankaitis (vytas@tamu.edu).

Materials availability—Plasmids generated in this study will be available upon reasonable request. This study did not generate any mouse lines that had not been previously described.

Data and code availability

- All data will be provided by the lead contact by request.
- This paper does not report original code.
- Any additional information required to reanalyze the data reported in this work paper is available from the lead contact upon request.

EXPERIMENTAL MODEL AND SUBJECT DETAILS

Mouse models—The mice used in this study are on the background of C57BL6 (for wild-type, *Pitpna*-floxed, *Pitpnb*-floxed, and *Emx1-Cre* strains), mixed A/C57BL6/C3H (for the *Vangl2 loop tail* line), or BALB/cByJ (for the *Celsr1 curly tail bobber* line). These mice were maintained in the animal facility of Texas A&M University Health Science Center, and handled in accordance with National Institute of Health and institutional guidelines on the care and use of animals. *Pitpna*-floxed and *Pitpnb*-floxed lines have been previously described (Xie et al., 2018). The *Emx1-Cre* line (Stock #005628, B6.129S2-*Emx1*$^{tm1(cre)Krj}$/J), *Vangl2 lp* line (Stock #000222, *LPT/LeJ*), and *Celsr1 ctb* line (Stock #016111, *CByJ.Cg-Celsr1*^{ctb}*/GrsrJ*) were procured from The Jackson Laboratory. For experiments involving floxed *Pitpna* and/or *Pitpnb*, littermate embryos with at least one non-floxed allele of *Pitpna* or *Pitpnb* were used as controls. For experiments involving *Vangl2*$^{lp/lp}$ or *Celsr1*$^{ctb/ctb}$ embryos, wild type or heterozygous littermate embryos were used as controls. For embryonic staging, the day of vaginal plug detection was designated as E0.5. Embryonic stages are indicated in figure legends. The sex of the embryos was not determined.

METHOD DETAILS

Plasmids—Plasmids for expression of EGFP (pCAX-EGFP), Cre (pCAG-Cre), and *Golph3* shRNA were previously described (Xie et al., 2018). To generate plasmids for the expression of PTK7ΔC, the coding sequence for PTK7 amino acid 1–728 (lacking the cytoplasmic domain) was amplified via RT-PCR from neocortex RNA preparations of E14.5 mouse embryos, and then inserted into the pCAX vector. To generate plasmids for the expression of MRLC2-AA (in which Thr18 and Ser19 of MRLC2 were mutated to Ala), the coding sequence for mouse gene *Myl12b* was amplified via RT-PCR from neocortex RNA preparations of E14.5 mouse embryos. *Myl12b* encodes mouse myosin regulatory

light chain, which is identical to human MRLC2. The coding sequence of *Myl12b* was then inserted into the pCAX vector, and T18A and S19A mutations were introduced into the plasmid via site-directed mutagenesis. RT-PCR was performed using iScript Select cDNA synthesis Kit (BIO-RAD) and high-fidelity Phusion DNA polymerase (New England Biolabs). The plasmid was verified by DNA sequencing.

Antibodies—The antibodies used include: rabbit polyclonal anti-GOLGIN97 (Abcam, ab98023), chicken polyclonal anti-GFP (Aves Labs, GFP-1010), mouse monoclonal anti-PAX6 (Developmental Studies Hybridoma Bank, PAX6), rabbit polyclonal anti-PAX6 (LSBio, LS-C179903 and LS-B16455), rabbit polyclonal anti-TBR2 (Abcam, ab183991), rat polyclonal anti-TBR2 (Thermo Fisher Scientific, 14-4875-82), sheep polyclonal anti-VANGL2 (Novus Biologicals, AF4815-SP), rabbit polyclonal anti-VANGL1 (Novus Biologicals, NBP1-86990), rabbit polyclonal anti-PTK7 (ProteinTech Group, 17799-1-AP), goat polyclonal anti-FZD2 (Novus Biologicals, NBP1-20920), goat polyclonal anti-PCNA (LSBio, B14132), rabbit polyclonal anti-pSer10 (GenScript, A00339), mouse monoclonal anti-BrdU (clone MoBu-1, Abcam, ab8039), and rabbit polyclonal anti-Ser19-phosphorylated MRLC2 (Cell Signaling, 3671S). Secondary antibodies (with minimal species cross reactivity) were from Jackson Immuno Research Laboratories, Inc (West Grove, PA).

In utero electroporation—In utero electroporation was performed as previously described (Xie et al., 2016, 2018). Briefly, timed-pregnant female mice were anesthetized and subjected to laparotomy to expose the uteri. The brain of mouse embryos was visualized using a fiber optic light source. Plasmid solutions were then injected into the lateral ventricle of the embryonic mouse brain through the uterine wall. Following plasmid injection, 5 short electric pulses were delivered across the head of mouse embryos. The uteri were then returned to the abdominal cavity of the dam, and the incision was sutured. The dam was allowed to recover at a warm location before being transferred to animal holding room. For *Pitpna*/*Pitpnb* knockout electroporation experiments, a mixture of pCAX-EGFP and pCAG-Cre (mass ratio of 1:2) was introduced into the neocortex of mouse embryos (*Pitpna*$^{fl/fl}$ *Pitpnb*$^{fl/fl}$ or *Pitpna*$^{+/+}$ *Pitpnb*$^{+/+}$) at E12.5, and electroporated embryos were harvested at E16.5. For GOLPH3 knockdown electroporation experiments, a mixture of pCAX-EGFP and Golph3 shRNA (mass ratio of 1:3) was introduced into the neocortex of wild-type mouse embryos at E12.5, and electroporated embryos were harvested a E15.5. For PTK7ΔC electroporation experiments, a mixture of pCAX-EGFP and pCAX-PTK7ΔC (mass ratio of 1:5) was introduced into the neocortex of wild-type mouse embryos at E12.5, and electroporated embryos were harvested 24h later. In experiments for analysis of lateral dispersion of NSCs, embryos were subjected to the first electroporation at E11.5, and the second electroporation 7h later.

BrdU/EdU/FlashTag pulse/chase analysis—Pregnant mice at the stage of E12.5 were administered with BrdU (50mg/kg) intraperitoneally, and anesthetized 2.5h later for CFSE labeling of the embryonic brain. About 1.5μl of low concentration CellTrace CFSE (50μg CFSE dissolved in 9μl of DMSO+135μl of PBS) was injected into the lateral ventricle of embryos. The use of this low concentration avoided prolonged presence of CFSE in

the lateral ventricle that would continuously label M-phase, and allowed the visualization of pure G1-phase cells 2.5h after CFSE injection (i.e. all pulse-labeled NSCs have exited M-phase 2.5h after injection). EdU (50mg/kg) was administered by intraperitoneal injection of the dam 1.5h after CFSE injection. Embryos were then sacrificed 1h after EdU administration. By this procedure, BrdU, CFSE, and EdU were administered to the embryos at 5h, 2.5h, and 1h, respectively, before harvest. Cryosections of the embryos were used for analysis of nuclear position. BrdU was detectd using the monoclonal antibody MoBu-1, which was previously shown to specifically recognize BrdU but not EdU (Bradford and Clarke, 2011). EdU was detected by a Click assay using the EZClick™ EdU Cell Proliferaion/DNA Synthesis Kit (BioVision).

Genotyping—Genomic DNA from mouse ear punching tissues was used for PCR genotyping. Taq DNA polymerase was used for genotyping PCR reactions. Genotyping for floxed *Pitpna*, floxed *Pitpnb*, and *Emx1-Cre* alleles was previously described (Xie et al., 2018). The following primers were used for genotyping the *ctb* line of *Celsr1* mice: Celsr1del1-F2wt (GTTCCTGGAGGTGTGAGC); Celsr1del1-F2del1 (GTTCCTGGAGGTGTGAGG); Celsr1del1-R2 (GAGCAGCTCCTGGAATCTTTG). The pair of Celsr1del1-F2wt and Celsr1del1-R2 detects the wild-type *Celsr1* allele (300bp; annealing temperature at 60°C), whereas the pair of Celsr1del1-F2del1 and Celsr1del1-R2 detects the mutant $Celsr1^{ctb}$ allele (300bp; annealing temperature at 60°C). For genotyping the *lp* line of *Vangl2* mice, a PCR product of 241bp encompassing the location of the *lp* mutation was amplified from the genomic DNA preparations using primers LpSeq-F (GAAAGCTGTGTCACAGAGGATG) and LpSeq-R (TCACTACCAAGCTGAAGTCCTG). The genotypes were determined by sequencing analysis of this PCR product.

Tissue preparation and immunostaining—For tissue sample preparation of E12.5 embryos, the whole brain was dissected out in PBS and fixed in 2% paraformaldehyde (in 1X PBS) for 20–30min. For tissue sample preparation of older embryos, forebrain hemispheres were dissected out, part of the hippocampus was removed to expose the lateral ventricle, and the rest of the forebrain was fixed in 2% paraformaldehyde (in 1X PBS) for 25–30min. Fixed forebrain samples were cryoprotected with 20% sucrose (in 1X PBS), embedded in Tissue-Tek OCT, and cryosectioned at the thickness of 20–30μm. Sections were stored at −20°C before the immunostaining procedure. For immunostaining, both primary and secondary antibodies were diluted in 1xPBS containing 3% bovine serum albumin and 0.2% Triton-X-100. Antibody incubation steps (primary antibody: overnight; secondary antibody: 1–3h) were performed in a humidified chamber protected from direct light. Secondary antibodies with the following cyanine dyes were used: Cy2 (green), Cy3 (red), Cy5 (far red), and DyLight405 (blue). EverBrite™ mounting media from Biotium (Fremont, CA) were used to mount coverslips and protect from photo bleaching.

Antigen retrieval treatment—Brain sections were subjected to antigen retrieval treatment prior to PCNA and pSer10 immunostaining. The procedure was performed similarly as previously described (Xie et al., 2016). Briefly, tissue sections were submerged in 1x antigen retrieval citrate solution (Sigma), microwaved for 5 min on power 90, left in the heated buffer for 5 min, and washed in 1x PBS three times prior to the immunostaining

procedure. After antigen retrieval treatment, many transfected cells that express EGFP at low to moderate levels are poorly visualized by EGFP immunoreactivity.

Confocal microscopy and immunoreactivity quantifications—Confocal images were obtained on a Nikon TiE confocal microscope using the NIS-Elements software. Quantification of relative immunoreactivity of VANGL2 was performed similarly as previously described for that of GOLPH3 (Xie et al., 2018). Briefly, Confocal images were converted to TIF files, which were then used for gray value measurement in Adobe Photoshop CS6. Cells from images obtained from at least three embryos were pooled together for each group. To quantify relative VANGL2 immunoreactivity at trans-Golgi for each transfected cell ($EGFP^+$), VANGL2 immunoreactivity at trans-Golgi (indicated by GOLGIN97 immunoreactivity) was compared to the thin layer of VANGL2 immunoreactivity surrounding the nucleus, which was consistent with the pattern of plasma membrane localization at the somata of NSCs.

QUANTIFICATION AND STATISTICAL ANALYSIS

The GraphPad Prism software (version 6.0b) was used for statistical analysis. Unpaired, two-tailed Student's t-test was used to compare results from two groups. One-way ANOVA were used to compare results from three or more groups. Details of statistical analyses, including statistical tests used, n values (n numbers and whether the n number represents mouse embryos or cells), and p values can be found in relevant figures and/or figure legends. Quantification data are represented as mean ± SD.

Supplementary Material

Refer to Web version on PubMed Central for supplementary material.

ACKNOWLEDGMENTS

This work was supported by NIH grant R35 GM131804 (to V.A.B.) and grant BE-0017 from the Robert A. Welch Foundation (to V.A.B.).

REFERENCES

Basu SN, Kollu R, and Banerjee-Basu S (2009). AutDB: a gene reference resource for autism research. Nucleic Acids Res 37, D832–D836. 10.1093/nar/gkn835. [PubMed: 19015121]

Bonnefont J, and Vanderhaeghen P (2021). Neuronal fate acquisition and specification: time for a change. Curr. Opin. Neurobiol 66, 195–204. 10.1016/j.conb.2020.12.006. [PubMed: 33412482]

Bradford JA, and Clarke ST (2011). Dual-pulse labeling using 5-ethynyl-2'-deoxyuridine (EdU) and 5-bromo-2'-deoxyuridine (BrdU) in flow cytometry. Curr. Protoc. Cytom 7, 7.38. 10.1002/0471142956.cy0738s55.

Butler MT, and Wallingford JB (2017). Planar cell polarity in development and disease. Nat. Rev. Mol. Cell Biol 18, 375–388. 10.1038/nrm.2017.11. [PubMed: 28293032]

Chen VS, Morrison JP, Southwell MF, Foley JF, Bolon B, and Elmore SA (2017). Histology atlas of the developing prenatal and postnatal mouse central nervous system, with emphasis on prenatal days E7.5 to E18.5. Toxicol. Pathol 45, 705–744. 10.1177/0192623317728134. [PubMed: 28891434]

Cleves AE, McGee TP, Whitters EA, Champlon KM, Aitken JR, Dowhan W, Goebl M, and Bankaitis VA (1991). Mutations in the CDP-choline pathway for phospholipid biosynthesis

bypass the requirement for an essential phospholipid transfer protein. Cell 64, 789–800. 10.1016/0092-8674(91)90508-v. [PubMed: 1997207]

Devenport D (2014). The cell biology of planar cell polarity. J. Cell Biol 207, 171–179. 10.1083/jcb.201408039. [PubMed: 25349257]

Di Donato N, Chiari S, Mirzaa GM, Aldinger K, Parrini E, Olds C, Barkovich AJ, Guerrini R, and Dobyns WB (2017). Lissencephaly: expanded imaging and clinical classification. Am. J. Med. Genet. A 173, 1473–1488. 10.1002/ajmg.a.38245. [PubMed: 28440899]

Ersoy I, Bunyak F, Chagin V, Cardoso MC, and Palaniappan K (2009). Segmentation and classification of cell cycle phases in fluorescence imaging. Med. Image Comput. Comput. Assist. Interv 12, 617–624. 10.1007/978-3-642-04271-3_75. [PubMed: 20426163]

Florio M, and Huttner WB (2014). Neural progenitors, neurogenesis and the evolution of the neocortex. Development 141, 2182–2194. 10.1242/dev.090571. [PubMed: 24866113]

Fumoto K, Uchimura T, Iwasaki T, Ueda K, and Hosoya H (2003). Phosphorylation of myosin II regulatory light chain is necessary for migration of HeLa cells but not for localization of myosin II at the leading edge. Biochem. J 370, 551–556. 10.1042/bj20021559. [PubMed: 12429016]

Gärtner S, Gunesch A, Knyazeva T, Wolf P, Högel B, Eiermann W, Ull-rich A, Knyazev P, and Ataseven B (2014). PTK 7 is a transforming gene and prognostic marker for breast cancer and nodal metastasis involvement. PLoS One 9, e84472. 10.1371/journal.pone.0084472. [PubMed: 24409301]

Gorski JA, Talley T, Qiu M, Puelles L, Rubenstein JLR, and Jones KR (2002). Cortical excitatory neurons and glia, but not GABAergic neurons, are produced in the Emx1-expressing lineage. J. Neurosci 22, 6309–6314. 10.1523/jneurosci.22-15-06309.2002. [PubMed: 12151506]

Govindan S, Oberst P, and Jabaudon D (2018). In vivo pulse labeling of iso-chronic cohorts of cells in the central nervous system using FlashTag. Nat. Protoc 13, 2297–2311. 10.1038/s41596-018-0038-1. [PubMed: 30258174]

Grabon A, Bankaitis VA, and McDermott MI (2019). The interface between phosphatidylinositol transfer protein function and phosphoinositide signaling in higher eukaryotes. J. Lipid Res 60, 242–268. 10.1194/jlr.r089730. [PubMed: 30504233]

Harris BS, Fairfield HE, Byers C, Ward Bailey PF, Berry ML, Yu H, Reinholdt LG, Donahue LR, Johnson KR, Bronson RT, et al. (2016). Two Spontaneous Alleles of *Celsr1*. MGI Direct Data Submission (MGI: J), p. 229303.

Hu WF, Chahrour MH, and Walsh CA (2014). The diverse genetic landscape of neurodevelopmental disorders. Annu. Rev. Genom. Hum. Genet 15, 195–213. 10.1146/annurev-genom-090413-025600.

Humphries AC, and Mlodzik M (2018). From instruction to output: Wnt/PCP signaling in development and cancer. Curr. Opin. Cell Biol 51, 110–116. 10.1016/j.ceb.2017.12.005. [PubMed: 29289896]

Insolera R, Bazzi H, Shao W, Anderson KV, and Shi SH (2014). Cortical neurogenesis in the absence of centrioles. Nat. Neurosci 17, 1528–1535. 10.1038/nn.3831. [PubMed: 25282615]

Juric-Sekhar G, and Hevner RF (2019). Malformations of cerebral cortex development: molecules and mechanisms. Annu. Rev. Pathol 14, 293–318. 10.1146/annurev-pathmechdis-012418-012927. [PubMed: 30677308]

Komatsu S, Yano T, Shibata M, Tuft RA, and Ikebe M (2000). Effects of the regulatory light chain phosphorylation of myosin II on mitosis and cytokinesis of mammalian cells. J. Biol. Chem 275, 34512–34520. 10.1074/jbc.m003019200. [PubMed: 10944522]

Kuna RS, and Field SJ (2019). GOLPH3: a Golgi phosphatidylinositol(4) phosphate effector that directs vesicle trafficking and drives cancer. J. Lipid Res 60, 269–275. 10.1194/jlr.r088328. [PubMed: 30266835]

Leung L, Klopper AV, Grill SW, Harris WA, and Norden C (2011). Apical migration of nuclei during G2 is a prerequisite for all nuclear motion in zebrafish neuroepithelia. Development 138, 5003–5013. 10.1242/dev.071522. [PubMed: 22028032]

Liang H, Hippenmeyer S, and Ghashghaei HT (2012). A Nestin-cre transgenic mouse is insufficient for recombination in early embryonic neural progenitors. Biol. Open 1, 1200–1203. 10.1242/bio.20122287. [PubMed: 23259054]

Lu X, Borchers AGM, Jolicoeur C, Rayburn H, Baker JC, and Tessier-Lavigne M (2004). PTK7/CCK-4 is a novel regulator of planar cell polarity in vertebrates. Nature 430, 93–98. 10.1038/nature02677. [PubMed: 15229603]

Lui JH, Hansen DV, and Kriegstein AR (2011). Development and evolution of the human neocortex. Cell 146, 332–336. 10.1016/j.cell.2011.07.005.

Miyama S, Takahashi T, Nowakowski RS, and Caviness VS Jr. (1997). A gradient in the duration of the G1 phase in the murine neocortical proliferative epithelium. Cereb. Cortex 7, 678–689. 10.1093/cercor/7.7.678. [PubMed: 9373022]

Miyata T, Okamoto M, Shinoda T, and Kawaguchi A (2015). Interkinetic nuclear migration generates and opposes ventricular-zone crowding: insight into tissue mechanics. Front. Cell. Neurosci 8, 473. 10.3389/fncel.2014.00473. [PubMed: 25674051]

Murdoch JN, Doudney K, Paternotte C, Copp AJ, and Stanier P (2001). Severe neural tube defects in the loop-tail mouse result from mutation of Lpp1, a novel gene involved in floor plate specification. Hum. Mol. Genet 10, 2593–2601. 10.1093/hmg/10.22.2593. [PubMed: 11709546]

Murdoch JN, Damrau C, Paudyal A, Bogani D, Wells S, Greene NDE, Stanier P, and Copp AJ (2014). Genetic interactions between planar cell polarity genes cause diverse neural tube defects in mice. Dis. Model. Mech 7, 1153–1163. 10.1242/dmm.016758. [PubMed: 25128525]

Nakagawa C, Senda-Murata K, Kawakita-Yamaguchi A, Fukada T, and Sugimoto K (2016). Molecular behavior of CENP-A and PCNA throughout the cell cycle in living human HT-1080 cells. Mol. Biol 5, 2.

Norden C, Young S, Link BA, and Harris WA (2009). Actomyosin is the main driver of interkinetic nuclear migration in the retina. Cell 138, 1195–1208. 10.1016/j.cell.2009.06.032. [PubMed: 19766571]

Okamoto M, Namba T, Shinoda T, Kondo T, Watanabe T, Inoue Y, Takeuchi K, Enomoto Y, Ota K, Oda K, et al. (2013). TAG-1-assisted progenitor elongation streamlines nuclear migration to optimize subapical crowding. Nat. Neurosci 16, 1556–1566. 10.1038/nn.3525. [PubMed: 24056697]

Parenti I, Rabaneda LG, Schoen H, and Novarino G (2020). Neurodevelopmental disorders: from genetics to functional pathways. Trends Neurosci 43, 608–621. 10.1016/j.tins.2020.05.004. [PubMed: 32507511]

Prigent C, and Dimitrov S (2003). Phosphorylation of serine 10 in histone H3, what for? J. Cell Sci 116, 3677–3685. 10.1242/jcs.00735. [PubMed: 12917355]

Qu Y, Glasco DM, Zhou L, Sawant A, Ravni A, Fritzsch B, Damrau C, Murdoch JN, Evans S, Pfaff SL, et al. (2010). Atypical cadherins celsr1–3 differentially regulate migration of facial branchiomotor neurons in mice. J. Neurosci 30, 9392–9401. 10.1523/jneurosci.0124-10.2010. [PubMed: 20631168]

Ravni A, Qu Y, Goffinet AM, and Tissir F (2009). Planar cell polarity cadherin Celsr1 regulates skin hair patterning in the mouse. J. Invest. Dermatol 129, 2507–2509. 10.1038/jid.2009.84. [PubMed: 19357712]

Rakic P (2009). Evolution of the neocortex: a perspective from developmental biology. Nat. Rev. Neurosci 10, 724–735. 10.1038/nrn2719. [PubMed: 19763105]

Reiner O, Sapir T, and Gerlitz G (2012). Interkinetic nuclear movement in the ventricular zone of the cortex. J. Mol. Neurosci 46, 516–526. 10.1007/s12031-011-9633-0. [PubMed: 21881827]

Schaaf G, Ortlund EA, Tyeryar KR, Mousley CJ, Ile KE, Garrett TA, Ren J, Woolls MJ, Raetz CR, Redinbo MR, and Bankaitis VA (2008). Functional anatomy of phospholipid binding and regulation of phosphoinositide homeostasis by proteins of the sec14 superfamily. Mol. Cell 29, 191–206. 10.1016/j.molcel.2007.11.026. [PubMed: 18243114]

Schenk J, Wilsch-Bräuninger M, Calegari F, and Huttner WB (2009). Myosin II is required for interkinetic nuclear migration of neural progenitors. Proc. Natl. Acad. Sci. U S A 106, 16487–16492. 10.1073/pnas.0908928106. [PubMed: 19805325]

Shindo A (2018). Models of convergent extension during morphogenesis. Wiley Interdiscip. Rev. Dev. Biol 7, e293. 10.1002/wdev.293.

Schönenberger F, Deutzmann A, Ferrando-May E, and Merhof D (2015). Discrimination of cell cycle phases in PCNA-immunolabeled cells. BMC Bioinf 16, 180. 10.1186/s12859-015-0618-9.

Sutherland A, Keller R, and Lesko A (2020). Convergent extension in mammalian morphogenesis. Semin. Cell Dev. Biol 100, 199–211. 10.1016/j.semcdb.2019.11.002. [PubMed: 31734039]

Strzyz PJ, Matejcic M, and Norden C (2016). Heterogeneity, cell biology and tissue mechanics of pseudostratified epithelia: coordination of cell divisions and growth in tightly packed tissues. Int. Rev. Cell Mol. Biol 325, 89–118. 10.1016/bs.ircmb.2016.02.004. [PubMed: 27241219]

Taverna E, Götz M, and Huttner WB (2014). The cell biology of neurogenesis: toward an understanding of the development and evolution of the neocortex. Annu. Rev. Cell Dev. Biol 30, 465–502. 10.1146/annurev-cellbio-101011-155801. [PubMed: 25000993]

Tsai JW, Chen Y, Kriegstein AR, and Vallee RB (2005). LIS1 RNA interference blocks neural stem cell division, morphogenesis, and motility at multiple stages. J. Cell Biol 170, 935–945. 10.1083/jcb.200505166. [PubMed: 16144905]

Vicente-Manzanares M, Ma X, Adelstein RS, and Horwitz AR (2009). Non-muscle myosin II takes centre stage in cell adhesion and migration. Nat. Rev. Mol. Cell Biol 10, 778–790. 10.1038/nrm2786. [PubMed: 19851336]

Waugh MG (2019). The Great Escape: how phosphatidylinositol 4-kinases and PI4P promote vesicle exit from the Golgi (and drive cancer). Biochem. J 476, 2321–2346. 10.1042/bcj20180622. [PubMed: 31462439]

Xie Z, Hur SK, Zhao L, Abrams CS, and Bankaitis VA (2018). A Golgi lipid signaling pathway controls apical Golgi distribution and cell polarity during neurogenesis. Dev. Cell 44, 725–740.e4. 10.1016/j.devcel.2018.02.025. [PubMed: 29587143]

Xie Z, Jones A, Deeney JT, Hur SK, and Bankaiis VA (2016). Inborn errors of long-chain fatty acid β-oxidation link neural stem cell self-renewal to autism. Cell Rep 14, 991–999. 10.1016/j.celrep.2016.01.004 [PubMed: 26832401]

Highlights

- PITPNA/PITPNB supports membrane trafficking of a subset of ncPCP receptors
- PITP/ncPCP stimulates actomyosin activity in neural stem cells in embryonic neocortex
- PITP/ncPCP-dependent actomyosin activity promotes interkinetic nuclear migration
- Interkinetic nuclear migration promotes lateral versus radial expansion of the neocortex

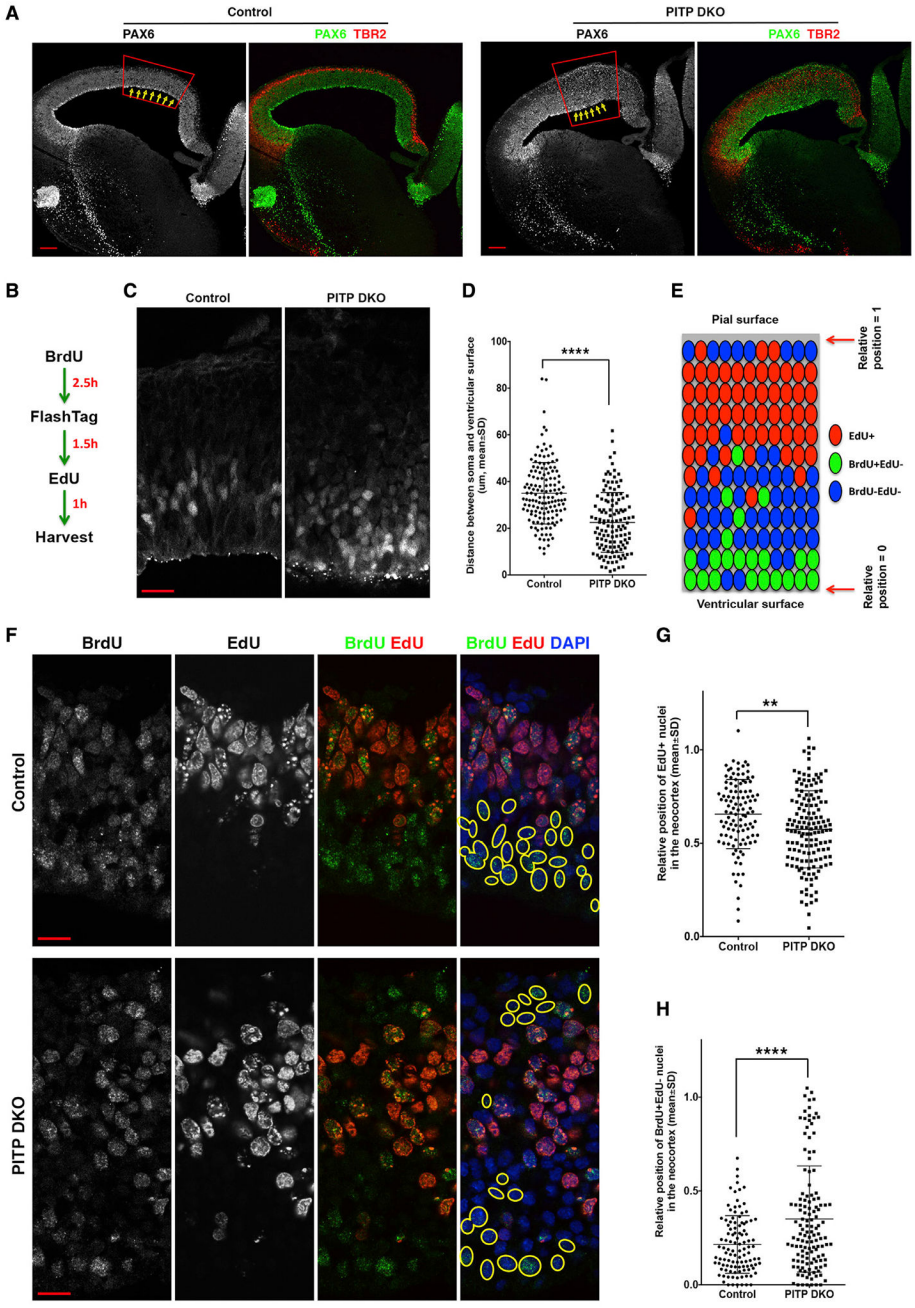

Figure 1. Altered neocortical shape and impaired IKNM in PITP DKO embryos

(A) Increased thickness (boxed areas) and convex ventricular surface (arrows) were observed in medial neocortex of PITP DKO embryos at late E12. Images are representative of at least 4 embryos for each group.

(B) Timeline of pulse-chase analysis of IKNM.

(C) Images of CFSE-labeled cells representative of 3 embryos for each group.

(D) Quantification. Cells (140 cells for control and 129 cells for PITP DKO) were pooled from 3 embryos for each group.

(E) Method for determining relative positions of EdU^+ and $BrdU^+EdU^-$ nuclei within the VZ.
(F) Images of EdU^+ and $BrdU^+EdU^-$ nuclei (yellow circles) representative of 3 embryos for each group.
(G) Quantification of EdU^+ nuclei. Nuclei (110 for control and 149 for PITP DKO) were pooled from 3 embryos for each group.
(H) Quantification of $BrdU^+EdU^-$ nuclei. Nuclei (109 for control and 132 for PITP DKO) were pooled from 3 embryos for each group.
**$p < 0.01$ and ****$p < 0.0001$, Student's t test. Scale bars: 100 μm (A), 20 μm (C), and 10 μm (F).

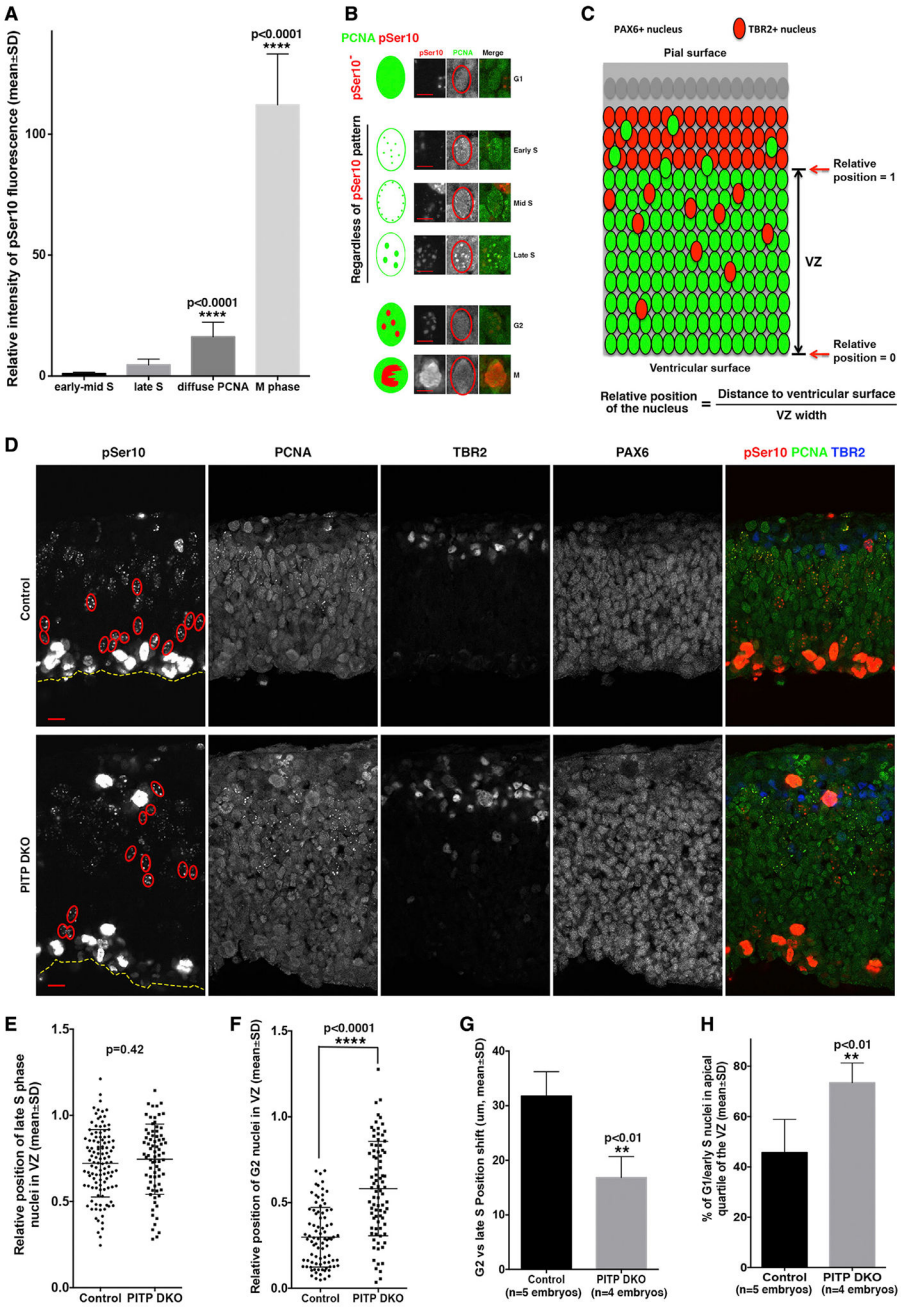

Figure 2. Analysis of IKNM defects by immunoreactivity of pSer10 and PCNA

(A) Intensity of pSer10 immunofluorescence in subpopulations of pSer10$^+$ NSCs at E12.5. NSCs (n = 35, 42, 34, and 27 cells for early-mid S, late S, diffuse PCNA, and M phase groups, respectively) were pooled from 3 embryos.

(B) Identification of cell cycle phases on the basis of fluorescence patterns of PCNA and pSer10. Schematic drawings are on the left, and actual representative images of nuclei (outlined by red circles) are on the right.

(C) Schematic for nuclear position quantification.

(D–H) IKNM defects in PITP DKO embryos revealed by quadruple immunostaining. Representative images of the medial neocortex are shown in (D). G2 nuclei (red circles) and the ventricular surface (dashed yellow lines) are outlined. Quantifications were performed at E12.5 (regardless of whether the stage was early or late E12). Quantifications for (E) (113 nuclei for control and 75 nuclei for PITP DKO) and (F) (86 nuclei for control and 83 nuclei for PITP DKO) represent NSC datasets pooled from at least 4 independent embryos for each group.

**$p < 0.01$ and ****$p < 0.0001$, one-way ANOVA (A) and Student's t test (E–H). Scale bars: 5 μm (B) and 10 μm (D).

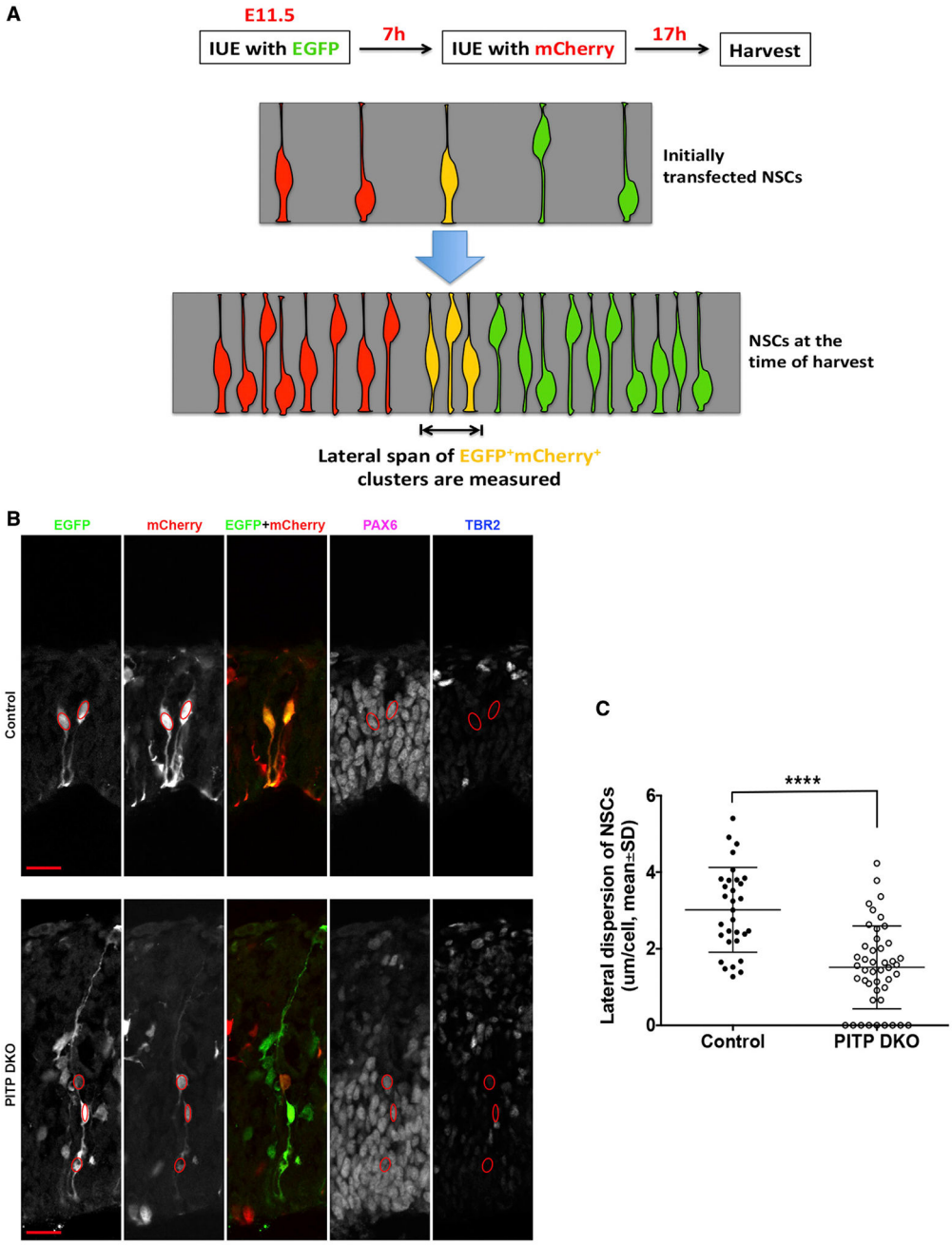

Figure 3. Reduced lateral dispersion of NSCs in PITP DKO embryos

(A) Schematic of the two-step electroporation assay.

(B) Images of doubly transfected NSC clusters ($EGFP^+mCherry^+PAX6^+TBR2^-$, nuclei indicated by red circles) in the medial neocortex representative of at least 3 embryos for each group. Scale bars: 20 μm.

(C) Quantification indicates significantly reduced lateral dispersion of NSCs in PITP DKO embryos. Datasets (31 NSC clusters for control and 45 NSC clusters for PITP DKO) were pooled from at least 3 embryos for each group.

****$p < 0.0001$, Student's t test.

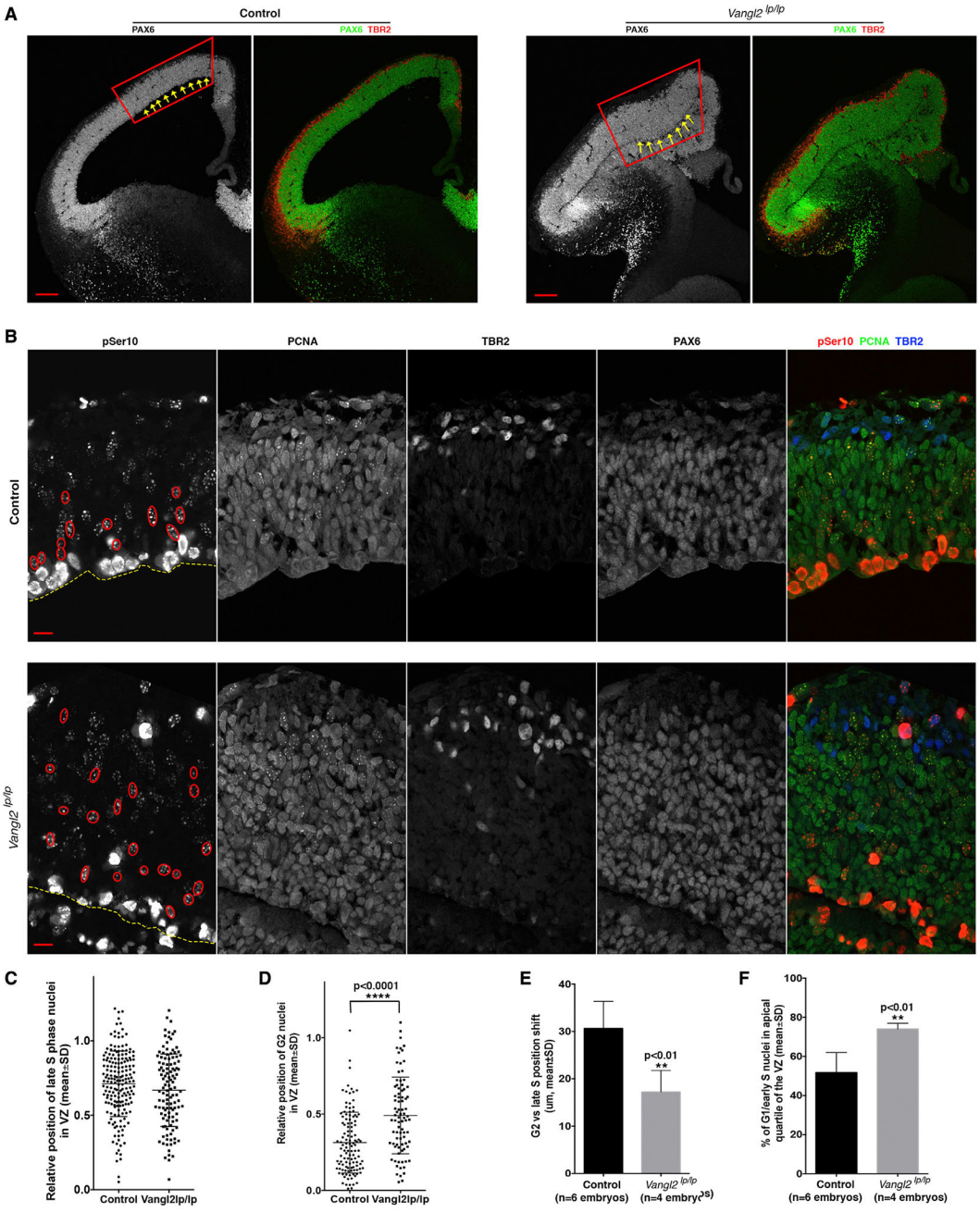

Figure 4. Altered neocortical shape and impaired IKNM in *Vangl2*$^{lp/lp}$ mutant embryos

(A) Increased neocortical thickness (boxed areas) and convex ventricular surface (arrows) were common in *Vangl2*$^{lp/lp}$ mutant embryos at E12.5, particularly in the medial neocortex. Images are representative of at least 5 embryos for each group.

(B–F) IKNM defects in *Vangl2*$^{lp/lp}$ mutant embryos at E12.5. (B) Images representative of at least 4 embryos for each group. Neocortical areas with increased thickness were examined for IKNM defects. G2 nuclei (red circle) and the ventricular surface (dashed yellow lines) are outlined. (C–F) Quantifications. Quantifications for (C) (183 nuclei for control and 118

nuclei for *Vangl2*$^{lp/lp}$) and (D) (117 nuclei for control and 85 nuclei for *Vangl2*$^{lp/lp}$) represent datasets pooled from at least 4 independent embryos for each group.

**p < 0.01 and ****p < 0.0001, Student's t test. Scale bars: 100 μm (A) and 10 μm (B).

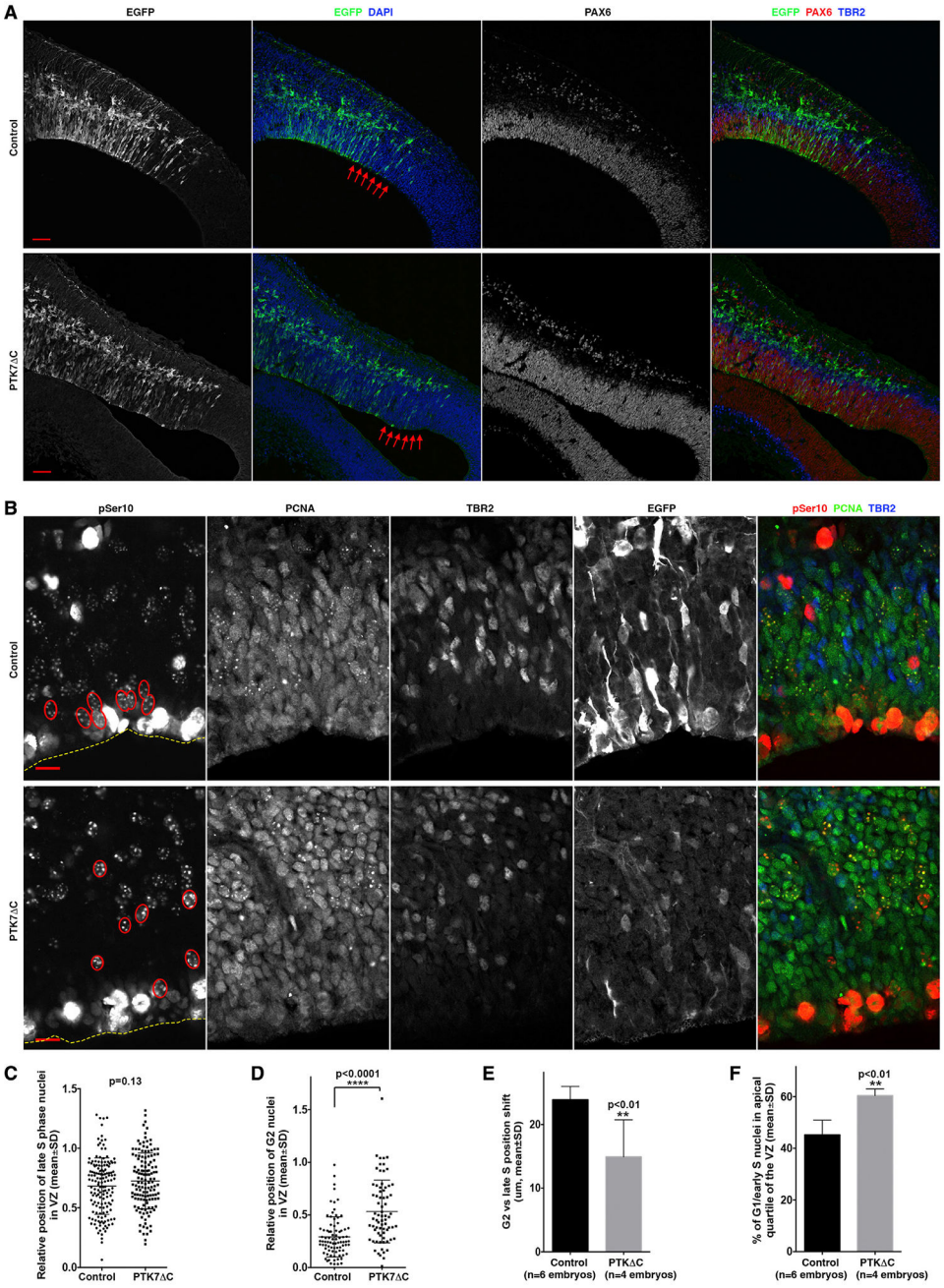

Figure 5. Mutant PTK7 causes increased thickness and convex ventricular surface in local neocortical areas

Wild-type embryos were electroporated with a PTK7ΔC plasmid and an EGFP plasmid at E12.5, and sacrificed 24 h later.

(A) PTK7ΔC caused localized neocortical shape changes. Arrows indicate an area of increased thickness of the neocortex accompanied with convex ventricular surface in a PTK7ΔC transfected embryo compared with control (EGFP plasmid only) transfected areas. Images are representative of 4 or more embryos for each group.

(B–F) IKNM defects in PTK7ΔC transfected neocortices. (B) Images representative of at least 4 embryos for each group. Transfected neocortical areas with increased thickness were

examined for IKNM defects. G2 nuclei (red) and the ventricular surface (dashed yellow lines) are outlined. PTK7ΔC did not affect positions of late S-phase NSC nuclei (C) (150 nuclei for control, 134 nuclei for PTK7ΔC) but shifted positions of G2-phase NSC nuclei (D) (84 nuclei for control, 73 nuclei for PTK7ΔC). Datasets were pooled from at least 4 independent embryos for each group. (E) The shift in position toward the ventricular surface in NSCs progressing from late S to G2 phase was reduced in PTK7ΔC-transfected neocortical areas. (F) The percentage of G1- and early S-phase NSC nuclei at the apical quartile of the VZ was increased in PTK7ΔC-transfected neocortical areas.
**$p < 0.01$ and ****$p < 0.0001$, Student's t test. Scale bars: 50 μm (A) and 10 μm (B).

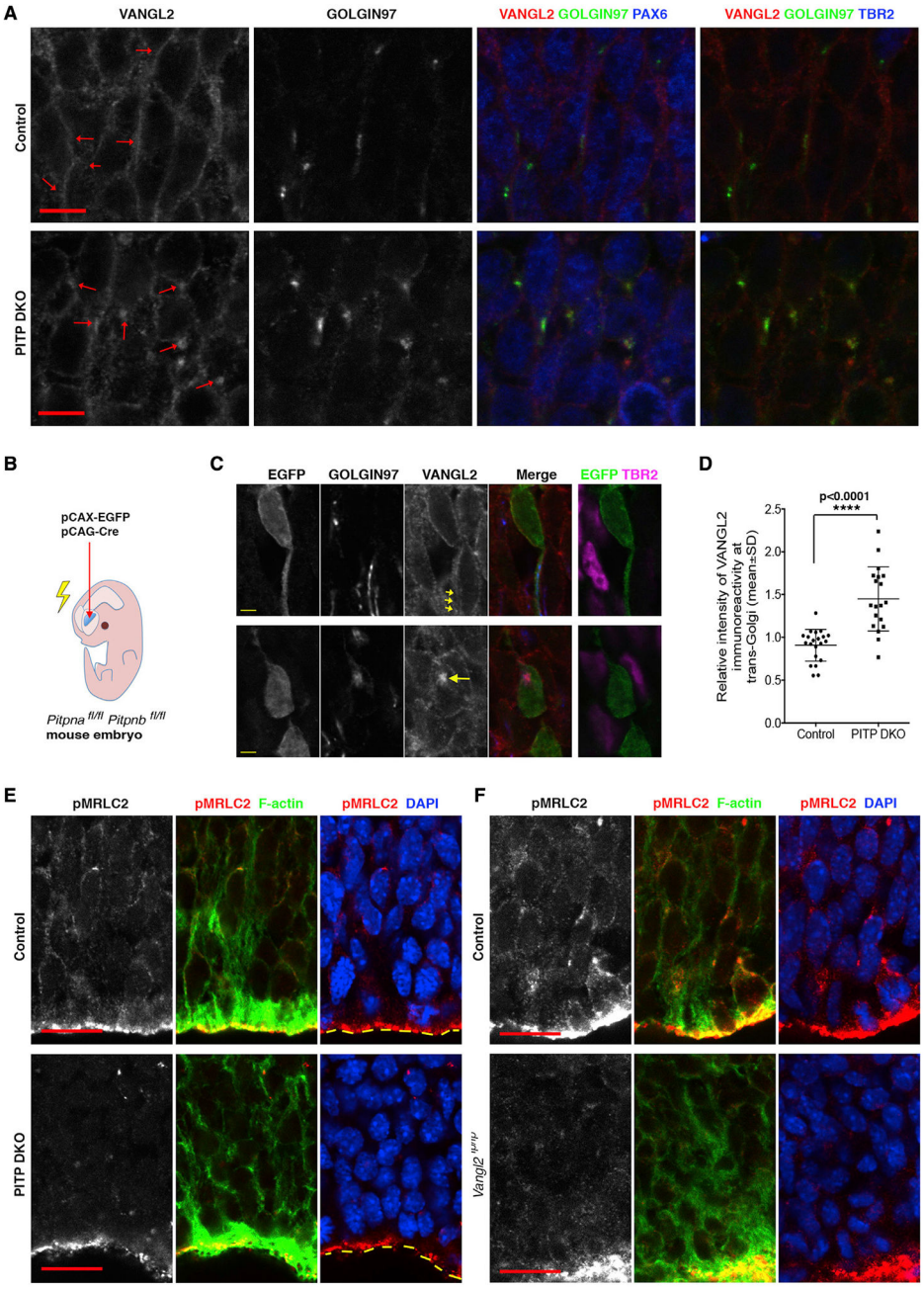

Figure 6. PITP deficiencies impaired VANGL2 membrane trafficking and actomyosin activity

(A) Accumulation of VANGL2 at *trans*-Golgi in NSCs in the medial neocortex of PITP DKO embryos at E12.5. Arrows indicate VANGL2 immunoreactivity at the NSC TGN (marked by GOLGIN97 labeling). Images are representative of at least 4 embryos for each group.

(B–D) Deleting *Pitpna* and *Pitpnb* in individual NSCs in otherwise normal neocortices leads to accumulation of VANGL2 at *trans*-Golgi. (B) Schematic for the experiment. Control (*Pipna*$^{+/+}$ *Pitpnb*$^{+/+}$) or *Pipna*$^{fl/fl}$ *Pitpnb*$^{fl/fl}$ mouse embryos were electroporated with an EGFP plasmid and a Cre plasmid at E12.5 and sacrificed at E16.5. (C) Images representative

of 3 embryos for each group. (D) Quantification. Transfected NSCs were identified as $EGFP^{+}TBR2^{-}$ cells located close to the ventricular surface. Datasets (21 NSCs for control, 19 NSCs for PITP DKO) were pooled from 3 embryos for each group. ****$p < 0.0001$, Student's t test.

(E and F) Actomyosin activity in E12.5 neocortices. The ventricular surface is outlined by yellow dashed lines. Images are representative of at least 4 embryos for each group. Actomyosin activity was reduced in areas surrounding the VZ nuclei in the neocortex of PITP DKO embryos (E) and *Vangl2*$^{lp/lp}$ embryos (F). Scale bars: 5 μm (A), 2 μm (C), and 10 μm (E and F).

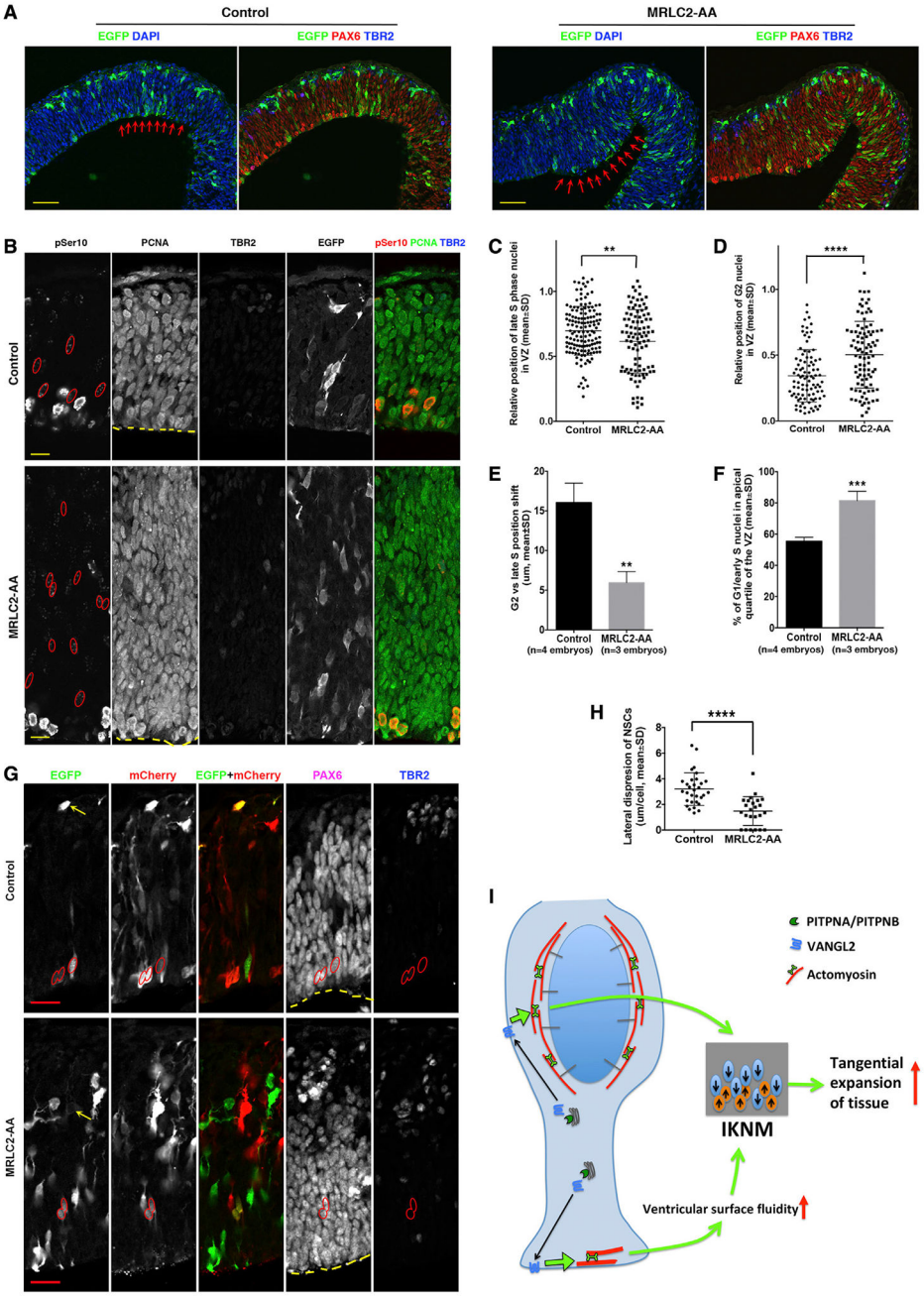

Figure 7. MRLC2-AA affects IKNM, neocortical shape, and lateral dispersion of NSCs

(A–F) Mouse embryos were electroporated with an EGFP plasmid and an MRLC2-AA plasmid at E11.5 and sacrificed 20 h later. (A) MRLC2-AA caused neocortical shape changes. Arrows indicate heavily transfected medial neocortical areas that exhibited increased thickness and a convex ventricular surface in MRLC2-AA group. Images are representative of at least 3 embryos for each group. (B–F) MRLC2-AA impaired IKNM. (B) Images representative of at least 3 embryos for each group. G2-phase NSCs (red circles) and the ventricular surface (yellow dashed lines) are outlined. (C–F) Quantifications. Cells were pooled from at least 3 embryos for each group. MRLC2-AA shifted late-S phase nuclei (140

nuclei for control and 96 nuclei for MRLC2-AA) toward the ventricular surface (C), shifted G2-phase nuclei (93 nuclei for control and 94 nuclei for MRLC2-AA) toward the basal side of the VZ (D), reduced the distance change when cells switch from late S-phase to G2 phase (E), and increased presence of G1- and early S-phase nuclei in the apical quartile of the VZ (F). (G and H) MRLC2-AA reduced lateral dispersion of NSCs. Mouse embryos were electroporated with an EGFP plasmid and an MRLC2-AA plasmid at E11.5, electroporated with an mCherry plasmid 7 h later, and sacrificed 17 h later.

(G) Images representative of at least 3 embryos for each group. The nuclei of doubly transfected NSC clusters (red circles) and the ventricular surface (yellow dashed lines) are outlined. Yellow arrows point to doubly transfected IPCs ($TBR2^+$, excluded for quantification).

(H) Quantification. Cell clusters (31 for control and 24 for MRLC2-AA) were pooled from at least 4 embryos for each group. **$p < 0.01$ and ****$p < 0.0001$, Student's t test.

(I) Model for the role of PITP/ncPCP signaling in IKNM and neocortical morphogenesis. PITPNA/PITPNB promote efficient trafficking of ncPCP receptors from *trans*-Golgi network to plasma membrane. ncPCP signaling supports IKNM by stimulating actomyosin activity around the nuclear periphery to directly promote IKNM, and/or by stimulating actomyosin activity at the apical tip to enhance ventricular surface fluidity that facilitates efficient IKNM. During IKNM, intercalation between G1 and G2 phase nuclei leads to preferential tissue expansion in the tangential dimension at the expense of radial tissue growth. Scale bars: 50 μm (A), 10 μm (B), and 20 μm (G).

KEY RESOURCES TABLE

REAGENT or RESOURCE	SOURCE	IDENTIFIER
Antibodies		
Chicken polyclonal anti-GFP	Aves Labs	Cat#GFP-1010; RRID:AB_2307313
Rabbit polyclonal anti-Ser10-phosphorylated histone H3	GenScript	Cat#A00339
Mouse monoclonal anti-PAX6	Developmental Studies Hybridoma Bank	RRID:AB_528427
rabbit polyclonal anti-PAX6	LSBio	Cat#LS-C179903 and #LS-B16455
Rabbit polyclonal anti-TBR2	Abcam	Cat#ab_183991; RRID:AB_2721040
Rat monoclonal anti-TBR2	Thermo Fisher Scientific	Cat# 14-4875-82; RRID:AB_11042577
sheep polyclonal anti-VANGL2	Novus Biologicals	Cat# AF4815-SP; RRID:AB_2272693
rabbit polyclonal anti-VANGL1	Novus Biologicals	Cat# NBP1-86990; RRID:11019907
rabbit polyclonal anti-PTK7	ProteinTech Group	Cat#17799-1-AP; RRID:2878442
goat polyclonal anti-FZD2	Novus Biologicals	Cat# NBP1-20920; RRID:1642086
goat polyclonal anti-PCNA	LSBio	Cat# B14132
Mouse monoclonal anti-BrdU (MoBU-1)	Abcam	Cat# ab8039 RRID:AB_306213
Rabbit polyclonal anti-MRLC2-pSer19	Cell Signaling Technology	Cat# 3671S AB_330248
Critical commercial assays		
iScript Select cDNA Synthesis Kit	BIO-RAD	Cat#170-8897
EZClick™ EdU Cell Proliferaion/DNA Synthesis Kit	BioVision	Cat# K946
Experimental models: Organisms/strains		
Mouse: *Pitpna$^{fl/fl}$ Pitpnb$^{fl/fl}$*	Xie et al. (2018)	
Mouse: *Emx1^{Cre}: B6.129S2-Emx1$^{tm1(cre)Krj}$/J*	The Jackson Laboratory	JAX:005628
Mouse: *LPT/LeJ*	The Jackson Laboratory	JAX:000222
Mouse: *CByJ.Cg-Celsr1^{ctb}/GrsrJ*	The Jackson Laboratory	JAX: 016111
Oligonucleotides		
Celsr1del1-F2wt: gttcctggaggtgtgagc	This manuscript	N/A
Celsr1del1-F2del1: gttcctggaggtgtgagg	This manuscript	N/A
Celsr1del1-R2: gagcagctcctggaatctttg	This manuscript	N/A
LpSeq-F: gaaagctgtgtcacagaggatg	This manuscript	N/A
LpSeq-R: tcactaccaagctgaagtcctg	This manuscript	N/A
Recombinant DNA		
pCAX-EGFP	Xie et al. (2016)	N/A
pCAG-Cre	Xie et al. (2018)	N/A
pSilencer-GOLPH3 shRNA	Xie et al. (2018)	N/A
pCAX-PTK7ΔC	This manuscript	N/A
pCAX-MRLC2-AA	This manuscript	N/A
Software and algorithms		
Nikon NIS Elements software package version 4.10	Nikon, Melville, NY	N/A
GraphPad Prism, Version 6.0b	GraphPad Software, Inc	N/A